Flow-Induced Non-Hermitian Sensing and Fundamental Capacity Budget

Qiang-Kai-Lai Huang[1,2,#], Yanxiang Wang[1,2,#], Pei-Chao Cao[1,2], Yuhan Zhong[1,2], Ran Ju[1,2,3], Dong Wang[1,2], Xiaochang Xing[1,2], Yifan Shou[1,2], Hanqi Chen[1,2], Wenduo Yu[1,2], Haoran Yan[1,2], Lianjie Li[1,2], Run Hu[4], Yihao Yang[1,2], Fei Gao[1,2], Rui Xi[5,6,†], Cheng-Wei Qiu[3], Hongsheng Chen[1,2,‡], & Ying Li[1,2,*]

[1]State Key Laboratory of Extreme Photonics and Instrumentation, Zhejiang Key Laboratory of Intelligent Electromagnetic Control and Advanced Electronic Integration, Zhejiang University, Hangzhou 310027, China

[2]International Research Center for Information Science and Electronic Engineering, The Electromagnetics Academy at Zhejiang University, Zhejiang University, Haining 314400, China

[3]Department of Electrical and Computer Engineering, National University of Singapore, Singapore 117583, Singapore

[4]School of Energy and Power Engineering, Huazhong University of Science and Technology, Wuhan 430074, China

[5]Hangzhou Institute of Technology, Xidian University, Hangzhou 311231, China

[6]National Key Laboratory of Radar Signal Processing, Xidian University, Xi'an 710071, China

[#]These authors contributed equally to this work.

e-mail[†,‡,*]: xirui@xidian.edu.cn; hansomchen@zju.edu.cn; eleying@zju.edu.cn

The Supplementary Information Includes:

Supplementary Note 1: Thermal Circuit Equivalent for Nodal Potential Energy

Thermal transport processes consist of both resistive and energy storage components, which can be modeled as distributed resistance and capacitance, respectively. Consequently, resistive-capacitive (RC) network diagrams are employed as modeling tools to analyze the flow of heat. In a thermal lattice, the reciprocal of resistance (conductance) represents the coupling component, while the capacitance corresponds to the potential component. In this note, we aim to derive the compact capacitance, or the potential component, of our model.

Within one period of our system, the cavity and pipe only perform conductive transport, which can be modeled as a series of first-order RC circuits, also known as the Cauer model. For the fluid part, containing both conductive and convective transport, one might consider it as a current source. However, since we periodically truncate the entire system, the fluid transport properties within one period should not be modeled as a current source. Otherwise, inflow and outflow boundary conditions would be required on both sides of the truncation to ensure mass conservation. In that case, the truncation would not be valid, as we would need to account for the effects outside this period. Therefore, the fluid part is more appropriately modeled as a passive thermal diode, which provides different transport resistances along and against the flow direction and protects the truncation. Adequate heat exchange should occur between the fluid and the pipe, so the capacitors of these two parts are connected in parallel. Meanwhile, the resistive part of the fluid links the two cavities directly. The equivalent thermal networks along and against the flow direction are shown in Fig. S1a and Fig. S1b, respectively.

Taking Fig. S1a as an example, Kirchhoff's current law can be written as

$$\begin{cases} \dfrac{T_{i-1}-T_{\mathrm{mid}}}{R_{\mathrm{pipe}}}+i\omega\left(C_{\mathrm{pipe}}+C_{\mathrm{fluid}}\right)T_{\mathrm{mid}}+\dfrac{T_i-T_{\mathrm{mid}}}{R_{\mathrm{cavity}}}=0 \\ \dfrac{T_{i-1}-T_i}{D_+}+\dfrac{T_{\mathrm{mid}}-T_i}{R_{\mathrm{cavity}}}+i\omega C_{\mathrm{cavity}}T_i=0. \end{cases} \tag{S1}$$

Where parameters T, R, ω, C, and D_+ represent temperature, thermal resistor, angular frequency, thermal capacitor, and forward conduction thermal resistance of the thermal diode, respectively. The impedance Z viewed from T_{i-1} is defined as

$$Z_{i-1} = \frac{T_{i-1}}{Q_{i-1}} = \frac{T_{i-1}}{-i\omega\left[C_{\text{pipe}}T_{\text{mid}} + C_{\text{fluid}}T_{\text{mid}} + C_{\text{cavity}}T_i\right]}. \tag{S2}$$

The resistors and capacitors can be easily derived by

$$\begin{cases} R\_ = \dfrac{L}{\kappa\_ A_c} \\ C\_ = \rho\_ c_p\_ V\_, \end{cases} \tag{S3}$$

Where L, κ, A_c, ρ, c_p, and V represent the heat transfer length, conductivity, heat transfer cross-sectional area, density, specific heat capacity at constant pressure, and volume, respectively. The subscript can be replaced by 'cavity', 'pipe', and 'fluid' (only for its capacitor). For the diode D, its forward and reverse thermal resistance can be derived by analyzing the temperature distribution along the fluid. Assuming that the heat transport is in the x-direction, with upstream at $x = 0$ and downstream at $x = L$, the temperature distribution along x is given by[1]

$$T(x) = T_u + \left(T_d - T_u\right)\frac{e^{vx/\alpha} - 1}{e^{vL/\alpha} - 1}. \tag{S4}$$

Here, T_{u}, T_{d}, v, and α denote the upstream temperature, downstream temperature, velocity, and diffusivity, respectively. The total heat flow rate along the velocity direction is given by

$$Q_t^+ = -\kappa_{\text{fluid}}\frac{\partial T(x)}{\partial x}A_c + \rho c_p v T(x) A_c = \rho c_p v A_c\left(T_u + \frac{T_u - T_d}{e^{vL/\alpha} - 1}\right). \tag{S5}$$

This equation only considers the upstream inflow enthalpy flow but not the downstream outflow enthalpy flow. Therefore, the net heat flow rate within a period is given by

$$Q_n^+ = Q_t^+ - \rho c_p v A_c T_d = \rho c_p v A_c\left(T_u - T_d\right)\frac{e^{vL/\alpha}}{e^{vL/\alpha} - 1}. \tag{S6}$$

In our system, the upstream temperature for the i-th cavity is T_{i-1}, and the downstream temperature is T_i. Thus, the forward conduction thermal resistance is

$$D_+ = \frac{T_{i-1} - T_i}{Q_n^+} = \frac{e^{vL/\alpha} - 1}{\rho c_p v A_c e^{vL/\alpha}}. \tag{S7}$$

The reverse conduction thermal resistance can simply be derived by replacing the velocity v in Eq. (S7) with $-v$, resulting in

$$D_- = \frac{T_i - T_{i-1}}{Q_n^-} = \frac{e^{vL/\alpha} - 1}{\rho c_p v A_c}. \tag{S8}$$

By simultaneously solving Eqs. (S1) and (S2) and substituting Eqs. (S3) and (S7) with the material/geometric parameters defined in the Methods section of the main text, the impedance-frequency curve can be derived, as shown in Fig. 2b of the main text. We fit a first-order RC circuit to this curve and obtain the first-order fitting parameters R_{fit} and C_{fit}. The compact node potential depends on the compact thermal capacitor, therefore, our compact parameter can be derived by $\rho c_p = C_{\text{fit}}/V$, where ρc_p, and V are the product of density and specific heat capacity at constant pressure, and the volume of the cavity, respectively. Thus far, we have made a compact approximation to equivalently represent the distributed heat capacitors within one period as a compact node, which can be summarized as

$$\rho c_p = \mathcal{W}\left(\rho_{\text{cavity}} c_{p_{\text{cavity}}}, \rho_{\text{fluid}} c_{p_{\text{fluid}}}, \rho_{\text{pipe}} c_{p_{\text{pipe}}}\right). \tag{S9}$$

Here, $\mathcal{W}$ represents a concise expression function of our compact approximation. We can apply the same equivalence to the thermal transport in the reverse fluid flow direction (Fig. S1b). The results are the same, as the only difference is between the fluid diode resistance D_+ and D_-. However, in this part, we only focus on the compact equivalence of the distributed heat capacitors, and the resistance value has little influence.

Supplementary Note 2: Minichannel Coupling and the System's Hamiltonian

The coupling term within this system can be divided into two parts: bulk couplings and boundary couplings. We plot the first three cavities in Fig S2 to derive coupling terms. The cavity's governing equation is the first law of thermodynamics:

$$\frac{\partial U}{\partial t} + W = \Phi + \left[\dot{m}_{\text{in}} \left(h + \frac{1}{2} v^2 + gz \right)_{\text{in}} - \dot{m}_{\text{out}} \left(h + \frac{1}{2} v^2 + gz \right)_{\text{out}} \right] dS \,. \tag{S10}$$

Where U, W, Φ, $m_{\text{in/out}}$, h, $\frac{1}{2}v^2$, gz and dS denote internal energy, power, net conduction heat flow rate, unit area inward/outward mass flux, specific enthalpy, kinetic energy term, potential energy term, and micro element of cross-sectional area perpendicular to the direction of flow velocity, respectively. Assuming that the system is not doing external work and that the kinetic and potential energy of the entry and exit nodes (cavities) remain unchanged, Eq. (S10) can be simplified as:

$$\frac{\partial U}{\partial t} = \Phi + \left(\dot{m}_{\text{in}} h_{\text{in}} - \dot{m}_{\text{out}} h_{\text{out}} \right) dS \,. \tag{S11}$$

The liquid fluid is incompressible with a slow velocity, so the growth rate of thermodynamic energy can be written as the rate of change in temperature:

$$\frac{\partial U}{\partial t} = \rho c_p \frac{\partial T}{\partial t} dV \,. \tag{S12}$$

Here, ρc_p is the compact product of density and specific heat capacity at constant pressure, derived from the thermal circuit equivalent method (Supplementary Note 1). Given that the conductivity of cavity (molybdenum) is much larger than that of the liquid metal, the temperature is approximately uniformly distributed in the yz direction. Hence, we only consider heat transfer along the x direction. For the conduction part, the heat flow rate is:

$$\Phi = \left(q_{\text{in}} - q_{\text{out}} \right) dS \,. \tag{S13}$$

Here, $q_{\text{in/out}}$ denotes the inflow/outflow heat flux along the x direction. The inflow enthalpy flow rate is:

$$\dot{m}_{\text{in}} h_{\text{in}} dS = \rho_{\text{fluid}} c_{p_{\text{fluid}}} v T dS \,. \tag{S14}$$

Due to the slow flow rate and small pressure changes, for simplicity, we do not include the pressure energy term when considering enthalpy. The outflow enthalpy flow rate in $x + dx$ is:

$$\dot{m}_{\text{out}} h_{\text{out}} dS = \rho_{\text{fluid}} c_{p_{\text{fluid}}} \left(T + \frac{\partial T}{\partial x} dx \right) \left(v + \frac{\partial v}{\partial x} dx \right) dS \,. \tag{S15}$$

Based on the continuity equation $\partial v / \partial x = 0$, the net enthalpy flow rate can be derived as:

$$\dot{m}_{\text{in}} h_{\text{in}} dS - \dot{m}_{\text{out}} h_{\text{out}} dS = -\rho_{\text{fluid}} c_{p_{\text{fluid}}} v \frac{\partial T}{\partial x} dx dS \,. \tag{S16}$$

Substituting Eqs. (S12), (S13), and (S16) into Eq. (S11), we obtain:

$$\rho c_p \frac{\partial T}{\partial t} dV = \left(q_{\text{in}} - q_{\text{out}} \right) dS - \rho_{\text{fluid}} c_{p_{\text{fluid}}} v \frac{\partial T}{\partial x} dx dS \,. \tag{S17}$$

In our system, we develop the thermal circuit equivalent method to transform the continuous system into the compact model (or tight-binding model), which means that the temperature is uniform within a cavity (node). Therefore, $\partial T_i / \partial x = 0$, where the subscript i denotes the i-th cavity, indicating the uniform temperature within a cavity. Consequently, Eq. (S17) can be simplified as

$$\rho c_p \frac{\partial T}{\partial t} dV = \left(q_{\text{in}} - q_{\text{out}} \right) dS \,. \tag{S18}$$

With uniform material parameters in the cavity domain, by integrating this equation on both sides and expanding the expression of heat flow rate, we get:

$$\frac{\partial T}{\partial t} = -\frac{\kappa_{\text{fluid}} A_c}{\rho c_p V} \left(\nabla_x T_{\text{in}} \bullet \vec{n}_{\text{in}} + \nabla_x T_{\text{out}} \bullet \vec{n}_{\text{out}} \right) . \tag{S19}$$

Here, A_c and V denote the cross-sectional area of the minichannel and the volume of the cavity, respectively. The unit normal vectors have $\vec{n}_{\text{in}} \cdot \vec{x} = 1$, $\vec{n}_{\text{out}} \cdot \vec{x} = -1$.

There is an explanation for why the temperature gradient in Eq. (S16) is 0, while the temperature gradient in Eq. (S18) can be non-zero. This is because the partial derivative of Eq. (S16) is defined within the node (i.e., cavity domain), and the temperature gradient within this domain is 0. In contrast, the temperature gradient in Eq. (S18) is defined at the inlet and outlet interfaces of cavity (i.e., coupling fluid domain), and the temperature gradient at the inlet and outlet boundaries is not 0.

The unknown term in Eq. (S19) is the temperature gradient within the coupling fluid. Based on the governing equation Eq. (S17), one can derive the steady-state temperature distribution along the pipe. For one coupling pipe (with T_i at $x = 0$ and T_{i+1} at $x = L_{\mathrm{pipe}}$), the temperature distribution is:

$$T(x) = T_i + (T_{i+1} - T_i)\frac{e^{vx/\alpha} - 1}{e^{vL_{\mathrm{pipe}}/\alpha} - 1}. \tag{S20}$$

Here, L_{pipe} is the length of the pipe, namely the distance between two compact sites. The inflow/outflow temperature gradient for the i-th cavity can thus be derived as

$$\begin{aligned} \nabla_x T_{\mathrm{in}} \bullet \vec{n}_{\mathrm{in}} &= \frac{v e^{vL_{\mathrm{pipe}}/\alpha}}{\alpha\left(e^{vL_{\mathrm{pipe}}/\alpha} - 1\right)}(T_i - T_{i-1}) \\ \nabla_x T_{\mathrm{out}} \bullet \vec{n}_{\mathrm{out}} &= \frac{v}{\alpha\left(e^{vL_{\mathrm{pipe}}/\alpha} - 1\right)}(T_i - T_{i+1}) \end{aligned}. \tag{S21}$$

Substituting Eq. (S21) into Eq. (S19), we can obtain the coupling equation for the i-th cavity:

$$\begin{aligned} \frac{\partial T_i}{\partial t} &= \frac{-\kappa_{\mathrm{fluid}} A_c}{\rho c_p V}\left[\frac{v e^{vL_{\mathrm{pipe}}/\alpha}}{\alpha\left(e^{vL_{\mathrm{pipe}}/\alpha} - 1\right)}(T_i - T_{i-1}) + \frac{v}{\alpha\left(e^{vL_{\mathrm{pipe}}/\alpha} - 1\right)}(T_i - T_{i+1})\right]. \\ &= h_+(T_{i-1} - T_i) + h_-(T_{i+1} - T_i) \end{aligned} \tag{S22}$$

The coupling coefficients are defined as:

$$\begin{cases} h_+ = \dfrac{\kappa_{\mathrm{fluid}} A_c}{\rho c_p V}\dfrac{v e^{vL_{\mathrm{pipe}}/\alpha}}{\alpha(e^{vL_{\mathrm{pipe}}/\alpha} - 1)} = \dfrac{A_c v e^{vL_{\mathrm{pipe}}/\alpha}}{V(e^{vL_{\mathrm{pipe}}/\alpha} - 1)} \\ h_- = \dfrac{\kappa_{\mathrm{fluid}} A_c}{\rho c_p V}\dfrac{v}{\alpha(e^{vL_{\mathrm{pipe}}/\alpha} - 1)} = \dfrac{A_c v}{V(e^{vL_{\mathrm{pipe}}/\alpha} - 1)}. \end{cases} \tag{S23}$$

From the coupling coefficient containing the parameter v, it can be seen that although the flow field in this model does not affect the equivalent temperature change of the compact cavity in the form of enthalpy change (convection), the flow field actually influences the temperature distribution and acts on the coupling cavity through conduction.

To quantify the degree of non-reciprocity in our thermal lattice, we examine the ratio of forward to backward coupling coefficients, $r^2 = h_+/h_- = e^{vL_{\mathrm{pipe}}/\alpha}$, as a function of the advective flow velocity v

(Fig. S3). As predicted by the convective-diffusive model, the coupling asymmetry exhibits an exponential growth with increasing v, demonstrating that the liquid-metal flow effectively acts as a tunable synthetic imaginary gauge field. This rapid divergence from reciprocity ($v = 0$) provides the physical basis for inducing a robust non-Hermitian skin effect (NHSE).

Now, we calculate the boundary couplings. For the inflow boundary, the orange part in Fig. S2, there is convective heat flow rate injected from the left side, and outflow conductive and convective heat flow rate on the right side. For the left side inflow enthalpy per unit time:

$$\dot{m}_{\mathrm{in}} h_{\mathrm{l}} dS = \rho_{\mathrm{fluid}} c_{p_{\mathrm{fluid}}} v T_{\mathrm{ustr}} dS \,. \tag{S24}$$

And the right side outflow enthalpy per unit time is:

$$\dot{m}_{\mathrm{out}} h_{\mathrm{r}} dS = \rho_{\mathrm{fluid}} c_{p_{\mathrm{fluid}}} v T_{\mathrm{b}} dS \,. \tag{S25}$$

Here, $h_{\mathrm{l/r}}$, T_{ustr}, and T_{b} are specific enthalpies on the left/right side, upstream temperature, and inflow boundary temperature, respectively. Based on Eq. (S20), the conductive heat flow rate on the right side is:

$$q_{\mathrm{d_r}} = -\kappa_{\mathrm{fluid}} \nabla_x T_{\mathrm{b}^+} = -\kappa_{\mathrm{fluid}} \frac{T_{\mathrm{l}} - T_{\mathrm{in}}}{e^{vL_{\mathrm{in}}/\alpha} - 1} \frac{v}{\alpha} = \frac{\kappa_{\mathrm{fluid}} v}{\alpha\left(e^{vL_{\mathrm{in}}/\alpha} - 1\right)} \left(T_{\mathrm{in}} - T_{\mathrm{l}}\right). \tag{S26}$$

Here, L_{in} denotes the length of the inflow pipe, and T_{l} is the temperature of the first cavity. Combining Eq. (S11) and Eqs. (S24)–(S26), one can derive the boundary temperature at steady state as:

$$T_{\mathrm{b}} = \frac{\rho_{\mathrm{fluid}} c_{p_{\mathrm{fluid}}} v A_c T_{\mathrm{ustr}} + \dfrac{\kappa_{\mathrm{fluid}} v A_c}{\alpha\left(e^{vL_{\mathrm{in}}/\alpha} - 1\right)} T_{\mathrm{l}}}{\rho_{\mathrm{fluid}} c_{p_{\mathrm{fluid}}} v A_c + \dfrac{\kappa_{\mathrm{fluid}} v A_c}{\alpha\left(e^{vL_{\mathrm{in}}/\alpha} - 1\right)}}. \tag{S27}$$

The boundary temperature is a weighted average of T_{ustr} and T_{l}. We can define the coefficient ratio as:

$$\gamma = \rho_{\mathrm{fluid}} c_{p_{\mathrm{fluid}}} v A_c \Big/ \frac{\kappa_{\mathrm{fluid}} v A_c}{\alpha\left(e^{vL_{\mathrm{in}}/\alpha} - 1\right)} = \frac{\rho_{\mathrm{fluid}} c_{p_{\mathrm{fluid}}} \left(e^{vL_{\mathrm{in}}/\alpha} - 1\right)}{\rho c_p}. \tag{S28}$$

Therefore, we have:

$$T_{\mathrm{b}} = \frac{\gamma}{\gamma + 1} T_{\mathrm{ustr}} + \frac{1}{\gamma + 1} T_{\mathrm{l}}. \tag{S29}$$

By substituting the experimental parameters shown in the method section of the main text, and letting $L_{\mathrm{in}} = L_{\mathrm{pipe}}/2$, we find that $\gamma \ll 1$, so $T_b \approx T_1$, which means there is almost zero coupling between the inflow boundary and the first cavity. When it comes to the outflow boundary, it satisfies $-\vec{x}\cdot\vec{q} = 0$, indicating zero coupling between the outflow environment and the last cavity.

Combining Eq. (S22) and the boundary coupling analysis, we can derive the Hamiltonian for the N-site-open-boundary system (i.e., Eq. (3) in the main text):

$$\widehat{H}_0 = i\begin{bmatrix} -h_- & h_- & & & \\ h_+ & -(h_+ + h_-) & h_- & & \\ & \ddots & \ddots & \ddots & \\ & & h_+ & -(h_+ + h_-) & h_- \\ & & & h_+ & -h_+ \end{bmatrix}_{N\times N}. \tag{S30}$$

In the experiment, no adiabatic boundary condition is imposed; instead, the system exchanges energy with its surroundings across every interface. Therefore, Eq. (S19) can be revised to:

$$\begin{aligned} \frac{\partial T_i}{\partial t} &= -\frac{\kappa_{\mathrm{fluid}} A_c \left(\nabla_x T_{\mathrm{in}} \bullet \vec{n}_{\mathrm{in}} + \nabla_x T_{\mathrm{out}} \bullet \vec{n}_{\mathrm{out}}\right) + S_{\mathrm{a}} h_{\mathrm{N}} (T_i - T_{\mathrm{a}})}{\rho c_p V} \\ &= h_+ \left(T_{i-1} - T_i\right) + h_- \left(T_{i+1} - T_i\right) + h_{\mathrm{a}} \left(T_{\mathrm{a}} - T_i\right), \end{aligned} \tag{S31}$$

Here, S_{a}, h_N, and T_{a} are the ambient heat exchange area, Newtonian heat transfer coefficient, and ambient temperature, respectively. $h_{\mathrm{a}} = S_{\mathrm{a}} h_{\mathrm{N}} / \left(\rho c_p V\right)$ is the ambient coupling coefficient. The Hamiltonian can be revised to:

$$\hat{H}_{\mathrm{a}} = i\begin{bmatrix} -(h_- + h_{\mathrm{a}}) & h_- & & & \\ h_+ & -(h_+ + h_- + h_{\mathrm{a}}) & h_- & & \\ & \ddots & \ddots & \ddots & \\ & & h_+ & -(h_+ + h_- + h_{\mathrm{a}}) & h_- \\ & & & h_+ & -(h_+ + h_{\mathrm{a}}) \end{bmatrix}_{N\times N}. \tag{S32}$$

Compared with the Hamiltonian in Eq. (S30), the spectrum in Eq. (S32) causes an offset of energy on the imaginary part. Therefore, we need to apply a shifted compensation to the experimental spectrum results, given that our theoretical analysis and simulations are all based on thermally insulated boundary conditions.

To elucidate the intrinsic link between convection-induced non-reciprocal transport and non-Hermitian topological properties, we perform a similarity transformation (imaginary gauge transformation)

to map the continuous thermal process onto a discrete non-Hermitian Hamiltonian and extract the equivalent imaginary gauge potential. Starting from the non-reciprocal coupling coefficients defined in Eq. (S23), we introduce the non-reciprocal strength:

$$r^2 = h_+ \Big/ h_- = e^{vL_{\text{pipe}}/\alpha}. \tag{S33}$$

This allows the implementation of a space-dependent diagonal transformation matrix,

$$S = \text{diag}(1, r, r^2, \ldots, r^{N-1}), \tag{S34}$$

serving as a similarity transformation to map the non-Hermitian Hamiltonian $\hat{H}_0$ in Eq. (S30) onto an effective Hermitian operator:

$$\hat{H}' = S^{-1}\hat{H}_0 S = i\begin{bmatrix} -h_- & h_{\text{eff}} & & & \\ h_{\text{eff}} & -(h_+ + h_-) & h_{\text{eff}} & & \\ & \ddots & \ddots & \ddots & \\ & & h_{\text{eff}} & -(h_+ + h_-) & h_{\text{eff}} \\ & & & h_{\text{eff}} & -h_+ \end{bmatrix}_{N\times N}. \tag{S35}$$

Under this transformation, the off-diagonal elements become symmetric:

$$h_{\text{eff}} = \sqrt{h_+ h_-} = \frac{A_c v}{2V \sinh\left(\dfrac{vL_{\text{pipe}}}{2\alpha}\right)}. \tag{S36}$$

The synthetic imaginary gauge potential g is then extracted as:

$$g = \ln(r) = \frac{vL_{\text{pipe}}}{2\alpha} = \frac{\text{Pe}}{2}, \tag{S37}$$

where Pe denotes the Péclet number within the minichannel. Consequently, the forward and backward coupling coefficients can be rigorously formulated in the canonical form:

$$\begin{cases} h_+ = h_{\text{eff}} e^{g} \\ h_- = h_{\text{eff}} e^{-g} \end{cases}, \tag{S38}$$

consistent with the paradigmatic Hatano-Nelson model.

It is noteworthy that in our convective thermal lattice, the effective symmetric coupling h_{eff} is not a static constant but explicitly depends on the flow velocity v. In paradigmatic theoretical models like the Hatano-Nelson model, the hopping amplitude and the imaginary gauge field are often treated as independent variables. However, in our physical implementation, the convective flow acts as a single physical tuning parameter that simultaneously governs both the non-reciprocal topological driving force (the imaginary gauge field $g \propto v$) and the reciprocal thermal exchange baseline (h_{eff}). In the limit of zero flow velocity ($v \to 0$), taking the Taylor expansion of the hyperbolic sine function yields

$$\lim_{v\to 0} h_{\text{eff}} = h_0 = \frac{A_c \alpha}{V L_{\text{pipe}}}, \tag{S39}$$

which flawlessly recovers the pure thermal diffusion. Consequently, h_{eff} can be redefined by the intrinsic conductive thermal coupling h_0 and imaginary gauge potential g:

$$h_{\text{eff}} = h_0 \frac{g}{\sinh(g)}. \tag{S40}$$

As v increases, the system develops a robust NHSE governed by $e^{\pm g}$, while the baseline coupling h_{eff} experiences a concomitant modulation. This coupled parameter dependency captures the dual role of advection in real-world thermal transport, ensuring the rigorous physical validity of our mapping from macroscopic thermodynamics to discrete non-Hermitian topologies.

Supplementary Note 3: Exact Solution of Generalized Boundary Conditions

When an arbitrary reciprocal boundary coupling τ is considered in our system, the Hamiltonian in Eq. (S30) is revised to:

$$\begin{aligned}\hat{H}_\tau &= i\begin{bmatrix} -(h_- + \tau) & h_- & & & \tau \\ h_+ & -(h_+ + h_-) & h_- & & \\ & \ddots & \ddots & \ddots & \\ & & h_+ & -(h_+ + h_-) & h_- \\ \tau & & & h_+ & -(h_+ + \tau) \end{bmatrix}_{N\times N} \\ &= i\sum_{n=1}^{N-1}\left[h_- \hat{c}_n^\dagger \hat{c}_{n+1} + h_+ \hat{c}_{n+1}^\dagger \hat{c}_n - (h_+ + h_-)\hat{c}_n^\dagger \hat{c}_n\right] + i(h_+ - \tau)\hat{c}_1^\dagger \hat{c}_1 - i(h_+ + \tau)\hat{c}_N^\dagger \hat{c}_N + i\tau\left(\hat{c}_1^\dagger \hat{c}_N + \hat{c}_N^\dagger \hat{c}_1\right),\end{aligned} \tag{S41}$$

with the eigenequation:

$$\hat{H}_\tau \left|\mathbf{\Psi}\right\rangle = \omega \left|\mathbf{\Psi}\right\rangle. \tag{S42}$$

Here, $|\mathbf{\Psi}\rangle = \Sigma_n \psi_n |n\rangle$ and $|n\rangle = \hat{c}_n^\dagger |0\rangle$. The bulk and boundary equations can be written as:

$$\begin{cases} ih_+\psi_{n-1} - i(h_+ + h_-)\psi_n + ih_-\psi_{n+1} = \omega\psi_n \quad (n = 2,3,...,N-1) \\ -i\left(h_- + \tau\right)\psi_1 + ih_-\psi_2 + i\tau\psi_N = \omega\psi_1 \\ ih_+\psi_{N-1} - i\left(h_+ + \tau\right)\psi_N + i\tau\psi_1 = \omega\psi_N. \end{cases} \tag{S43}$$

The above governing equation can be expanded to the following boundary equation:

$$\begin{cases} h_+\psi_0 - h_+\psi_1 + \tau\psi_1 - \tau\psi_N = 0 \\ h_-\psi_{N+1} - h_-\psi_N + \tau\psi_N - \tau\psi_1 = 0. \end{cases} \tag{S44}$$

Based on translational symmetry, the wave function can be written as:

$$\left|\mathbf{\Psi}\right\rangle = \left(z_i, z_i^2, z_i^3, ..., z_i^{N-1}, z_i^N\right)^T. \tag{S45}$$

By inserting Eq. (S45) into the bulk equation in Eq. (S43), we obtain:

$$\omega = i\left[\frac{h_+}{z_i} + h_- z_i - \left(h_+ + h_-\right)\right]. \tag{S46}$$

It can be found that for a certain ω, there should be two roots corresponding to z_i (i.e., z_1 and z_2). According to Vieta's theorem, the relation between these two roots can be derived as:

$$z_1 z_2 = \frac{h_+}{h_-}. \tag{S47}$$

The expansion coefficient must be a combination of z_1 and z_2:

$$\psi_n = c_1 z_1^n + c_2 z_2^n. \tag{S48}$$

Substituting Eq. (S48) into Eq. (S44), and choosing $(c_1, c_2)^T$ as the expansion basis, we can derive the boundary matrix:

$$H_\mathrm{b} = \begin{bmatrix} h_+ - \left(h_+ - \tau\right)z_1 - \tau z_1^N & h_+ - \left(h_+ - \tau\right)z_2 - \tau z_2^N \\ h_- z_1^{N+1} - \left(h_- - \tau\right)z_1^N - \tau z_1 & h_- z_2^{N+1} - \left(h_- - \tau\right)z_2^N - \tau z_2 \end{bmatrix}. \tag{S49}$$

Since c_1 and c_2 should not be zero at the same time, the determinant of the boundary matrix must be zero:

$$\begin{aligned} &h_+h_-\left(z_2^{N+1}-z_1^{N+1}\right)-h_+\left(h_--\tau\right)\left(z_2^N-z_1^N\right)-\tau h_+\left(z_2-z_1\right)-h_-\left(h_+-\tau\right)\left(z_1z_2^{N+1}-z_2z_1^{N+1}\right)\\ &+\left(h_+-\tau\right)\left(h_--\tau\right)\left(z_1z_2^N-z_2z_1^N\right)-\tau h_-\left(z_1^Nz_2^{N+1}-z_2^Nz_1^{N+1}\right)+\tau^2\left(z_1^Nz_2-z_2^Nz_1\right)=0. \end{aligned} \tag{S50}$$

Considering the Bloch theorem:

$$z_1=re^{i\theta},\ z_2=re^{-i\theta}, \tag{S51}$$

along with Eq. (S47), we have:

$$r=\sqrt{\frac{h_+}{h_-}}=e^g. \tag{S52}$$

Here, r^2 is the non-reciprocal coefficient in our system. Substituting Eqs. (S51), (S52) into Eq. (S46), the eigenfrequency is given by:

$$\omega=-i\left(h_++h_-\right)+2i\sqrt{h_+h_-}\cos\theta, \tag{S53}$$

where θ is the undetermined coefficient. The exact value of θ can be derived from the boundary conditions. Substituting the Bloch's solution into the boundary conditions Eq. (S50), we obtain:

$$\begin{aligned} &h_+h_-r^{N+1}\sin\left[\left(N+1\right)\theta\right]-\left[h_+\left(h_--\tau\right)r^N+h_-\left(h_+-\tau\right)r^{N+2}\right]\sin\left(N\theta\right)\\ &+\left[h_+h_--\tau\left(h_++h_-\right)\right]r^{N+1}\sin\left[\left(N-1\right)\theta\right]-\tau\left(h_+r+h_-r^{2N+1}\right)\sin\theta=0. \end{aligned} \tag{S54}$$

The θ calculated from Eq. (S54) assists in determining the eigenfrequencies using Eq. (S53). Note that our Hamiltonian has the rank of $N-1$. This can be shown by transforming Eq. (S41) into row-echelon form:

$$R\left(\hat{H}_\tau\right)=\begin{bmatrix} 1 & & & & -1\\ & 1 & & & -1\\ & & \ddots & & \vdots\\ & & & 1 & -1\\ 0 & 0 & \cdots & 0 & 0 \end{bmatrix}_{N\times N}. \tag{S55}$$

We can see that the rank of this Hamiltonian is $N-1$, indicating that one eigenfrequency equals to zero. For a linear N-site system, there will be N eigenfrequencies. Therefore, one of them equals to zero, and the other $N-1$ eigenfrequencies can be derived from Eqs. (S54) and (S53). These eigenfrequencies are our exact analytical solutions, plotted as red dots in Fig. 3a (I–IV).

We first consider the open boundary condition (OBC), which means the parameter τ equals zero. Eq. (S54) can be simplified as:

$$2r\sin\left(N\theta\right)\cos\theta-\left(1+r^2\right)\sin\left(N\theta\right)=0. \tag{S56}$$

This equation should work in different r, which means:

$$\theta=\frac{m\pi}{N}\ \left(m\in\mathbb{Z}\right). \tag{S57}$$

Again, we have N eigenfrequencies, and one must be zero. Thus, the total eigenfrequencies can be represented as:

$$\omega_m=\begin{cases}-i(h_++h_-)+2i\sqrt{h_+h_-}\cos\dfrac{m\pi}{L} & m=1,2,3,...,L-1\\ 0 & m=L\end{cases}. \tag{S58}$$

We can see that all θ in OBC are real numbers, making the eigenfrequencies purely imaginary. These eigenfrequencies serve as the theoretical OBC spectrum, plotted as blue downward-pointing triangles in Fig. 2c. Now, let us discuss the eigenstates. In our non-reciprocal system where $r\neq1$, according to Eq. (S49), we have:

$$c_1=c_2\frac{z_2-1}{1-z_1}. \tag{S59}$$

Therefore,

$$\begin{aligned}\psi_n&=c_1z_1^n+c_2z_2^n\\&=-2ic_2r^n\left[e^{in\theta}\frac{r\sin\theta}{1-re^{i\theta}}+\sin\left(n\theta\right)\right]\end{aligned} \tag{S60}$$

We find that when $\theta=\frac{\pi}{2}$, i.e., $m=\frac{N}{2}$ (where N needs to be even), the Bloch wave vectors of the $\frac{N}{2}$-th eigenvalue will have a π phase difference. This property can be seen from the effective Bloch Hamiltonian of $\widehat{H}_0$:

$$\hat{H}_{\text{eff}}\left(k\right)=2i\sqrt{h_+h_-}\cos\left(k\right). \tag{S61}$$

The transformation basis from real space to momentum space is based on the generalized Bloch theory $k \to k - i\ln r$. The band structure of Eq. (S61) has a symmetric point at $\frac{\pi}{2}$, indicating the standing wave solution at this point. If the number of eigenfrequencies is odd, this symmetry point can be reached. However, considering that the rank of our real space Hamiltonian is $N-1$, we need to let the site number be even. Therefore, the $\frac{\pi}{2}$ symmetric point ($\frac{N}{2}$-th eigenfrequency) can be reached.

Eq. (S61) illustrates the one-band spectrum of our system. This symmetry can also be proved by combining two sites into a supercell. Consequently, the effective Hamiltonian in Eq. (S61) can be transformed into a second-order case:

$$\hat{H}(k) = i\begin{bmatrix} 0 & h_-\left(1+e^{-ik}\right) \\ h_+\left(1+e^{ik}\right) & 0 \end{bmatrix}. \tag{S62}$$

Owing to band folding, the amplification factor of the generalized Bloch wave vector is $r' = r^2 = \frac{h_+}{h_-}$. The effective Hamiltonian exhibits chiral symmetry, $\sigma_z \hat{H}'_{\text{eff}} \sigma_z = -\hat{H}'_{\text{eff}}$, which allows the zero mode to emerge when the site length N is odd. However, since our model has a rank of $N-1$, the site number needs to be even to reach the symmetric point.

The symmetric point's eigenvalue will be the lattice potential (zero mode for effective Hamiltonian), and its eigenstate will have a simple expression:

$$\omega_{N/2} = -i\left(h_+ + h_-\right) \tag{S63}$$

$$\left|\boldsymbol{\Psi}_{N/2}\right\rangle = \sum\nolimits_n \left(-r^2\right)^{\lfloor n/2 \rfloor} \left|n\right\rangle. \tag{S64}$$

Using the same method, the $(N/2)$-th intrinsic left vector of this point is:

$$\left\langle \boldsymbol{\Gamma}_{N/2}\right| = \sum\nolimits_n (-1)^{\lfloor n/2 \rfloor} \left(r^{-2}\right)^{\lceil (n/2)-1 \rceil} \left\langle n\right|. \tag{S65}$$

Here, $\lceil\cdot\rceil$ and $\lfloor\cdot\rfloor$ represent the ceiling and floor operations respectively.

Now, we turn to the case with non-zero reciprocal boundary coupling τ. In this case, Eq. (S54) can be rewritten as:

$$\eta_1 \sin\left[\left(N+1\right)\theta\right]-\eta_2 \sin\left(N\theta\right)+\eta_3 \sin\left[\left(N-1\right)\theta\right]=\eta_4 \sin\theta\,, \tag{S66}$$

where the coefficients are given by:

$$\begin{aligned}
\eta_1 &= h_+ h_- r^{N+1} \\
\eta_2 &= h_+\left(h_- -\tau\right) r^N + h_-\left(h_+ -\tau\right) r^{N+2} \\
\eta_3 &= \left[h_+ h_- -\tau\left(h_+ + h_-\right)\right] r^{N+1} \\
\eta_4 &= \tau\left(h_+ r + h_- r^{2N+1}\right).
\end{aligned} \tag{S67}$$

Making a trigonometric expansion to Eq. (S66):

$$\left(\eta_1+\eta_3\right)\sin\left(N\theta\right)\cos\left(\theta\right)+\left(\eta_1-\eta_3\right)\cos\left(N\theta\right)\sin\left(\theta\right)-\eta_2 \sin\left(N\theta\right)=\eta_4 \sin\theta\,. \tag{S68}$$

We consider the left side of Eq. (S68) to be the function $f_1(N,\theta)$, and its right side to be $f_2(N,\theta)$. Therefore, the values of θ are the intersection points of f_1 and f_2. We plot the curves of f_1 and f_2 with the variable θ depicted in Fig. S4. When the parameters N and τ are in a proper region, such as IV, VII, VIII in Fig. S4. There are $N-1$ intersection points in the region $\theta \in (0,\pi)$, indicating a purely imaginary spectrum (like the spectrum in Fig. 3a I and II). When N or τ increase, as seen in I, V and IX in Fig. S4, the pink and blue lines are tangent at the first intersection point, meaning the first two eigenfrequencies are degenerate. When N and τ continue to increase, as seen in II, III and VI in Fig. S4, the number of intersection points in $(0,\pi)$ is less than $N-1$, which means more eigenenergies are degenerated, and θ has complex solutions, indicating a complex spectrum (like Fig. 3a III and IV).

The above intersection picture also provides a direct numerical route to the finite-size critical coupling without invoking any large-N approximation. Specifically, for a given N and non-reciprocal strength, the critical point can be obtained by solving the generalized boundary condition (GBC) equation together with the tangency condition,

$$f_1(N,\theta;\tau)=f_2(N,\theta;\tau),\partial_\theta f_1(N,\theta;\tau)=\partial_\theta f_2(N,\theta;\tau), \tag{S69}$$

or equivalently $F(\theta,\tau)=0$ and $\partial_\theta F(\theta,\tau)=0$. This procedure can be implemented numerically, to obtain the finite-size GBC threshold $\tau_{\max}$ with no assumption on the thermodynamic limit. The resulting values

are used as the exact GBC predictions in the main text. To obtain a compact analytical scaling law, we next focus on the middle intrinsic states and introduce the following controlled approximation.

To obtain a closed-form expression for the critical coupling $\tau_{\max}$ corresponding to the degeneracy of the middle intrinsic states (i.e., the $N/2$-th states), we apply the tangency condition to the N-τ relation. For these mid-spectrum states, the degeneracy occurs near the centre of the Brillouin zone, which corresponds to the phase angle $\theta = \frac{\pi(N-1)}{2N} \approx \frac{\pi}{2}$:

$$f_1\left(\theta = \frac{\pi}{2}\right) = f_2\left(\theta = \frac{\pi}{2}\right). \tag{S70}$$

Expanding this equation, we have

$$\tau_{\max} = \frac{h_+ h_- (r^N + r^{N+2}) \sin(N\theta)}{(h_+ + h_-) r^{N+1} \cos(N\theta) + (h_+ r^N + h_- r^{N+2}) \sin(N\theta) - (h_+ r + h_- r^{2N+1})}. \tag{S71}$$

Where $\tau_{\max}$ denotes the critical coupling strength beyond which the $N/2$-th eigenvalue enters the degenerate regime. The analytical solution provided in Eq. (S71) is represented by the grey dashed line in the color maps of Figs. S5 and S6, demonstrating excellent agreement with the upheaval of S. By substituting Eqs. (S36), (S38), and (S52) into Eq. (S71), we can simplify the expression for the maximum boundary coupling threshold as follows:

$$\tau_{\max} = \frac{h_{\text{eff}} (r + r^{-1}) \sin(N\theta)}{(r + r^{-1}) \cos(N\theta) + 2 \sin(N\theta) - (r^{N-1} + r^{-(N-1)})} \tag{S72}$$

At this stage, a critical distinction must be made regarding the phase variable θ to resolve the finite-size quantization. The expression derived above contains the term $N\theta$, which acts as a "fast-oscillating" phase variable governed by the boundary conditions, while the "slow" envelope variable θ has already been approximated as $\pi/2$ (Eq. (S70)). Directly substituting $\theta = \pi/2$ into the fast variable $N\theta$ would erroneously yield 0 for certain even configurations of N, physically implying a zero-coupling threshold. This paradox is resolved by recalling the phase transition criterion: the degeneracy emerges precisely when the spectral curves are tangent to each other. Mathematically, this tangency necessitates evaluating the expression at the local extrema of the oscillatory functions, which dictates the strict condition $\sin N\theta = \pm 1$

and $\cos N\theta = 0$. To yield a physically meaningful (positive) boundary coupling threshold $\tau_{\max}$, we must select the negative extremum $\sin N\theta = -1$. Substituting these tangency conditions into the expression, we obtain the finite-size critical threshold for the $N/2$-th state:

$$\tau_{\max} \approx \frac{h_{\text{eff}}(r + r^{-1})}{2 + (r^{N-1} + r^{-(N-1)})} \tag{S73}$$

To unveil the underlying scaling behavior, we evaluate Eq. (S73) in the macroscopic limit where both the site number N and the imaginary gauge potential g are sufficiently large. Thus, the exact expression elegantly simplifies to the asymptotic scaling law:

$$\tau_{\max} \approx h_{\text{eff}} e^{-|g|(N-2)}. \tag{S74}$$

By non-dimensionalizing the coupling coefficients τ with respect to the intrinsic conductive thermal coupling h_0 defined in Eq. (S39), i.e., introducing $\tilde{\tau} = \tau/h_0$, the upper expression can be rewritten as:

$$\tilde{\tau}_{\max} = \frac{h_{\text{eff}}}{h_0} e^{-|g|(N-2)} = \frac{g}{\sinh(g)} e^{-|g|(N-2)}. \tag{S75}$$

In the large-N regime, the relative variation of the algebraic prefactor $g/\sinh g$ becomes negligible. Therefore, the behavior of the dynamic range undergoes a near-exponential decay with respect to both the site number N and the strength of the synthetic imaginary gauge field g. This characteristic decay is a universal hallmark of non-Hermitian systems driven by a directional bias. Physically, the non-reciprocal lattice acts as a multi-stage directional pump; as N and g increase, the total non-reciprocal gain across the lattice scales exponentially (Eq. (S64)). The boundary coupling τ effectively introduces a feedback loop into this "amplifier," and a topological phase transition is triggered when this feedback becomes sufficient to restore macroscopic circulation—thereby collapsing the OBC spectral features into PBC loops. Because the "pumped" signal is amplified by a factor of $e^{N|g|}$, it universally requires only an exponentially small boundary perturbation, scaled precisely by $e^{-N|g|}$, to bridge the open boundaries and destroy the skin modes. This inherent "fragility" of the non-Hermitian skin effect serves as the fundamental constraint on the dynamic range of our sensing system.

Supplementary Note 4: Non-Hermitian Perturbation Theory and Fundamental Sensing Trade-off

For the non-Hermitian Hamiltonian $\widehat{H}_\tau$, its eigenequations are given by:

$$\begin{cases} \hat{H}_\tau \left|\mathbf{\Psi}_n\right\rangle = \omega_n \left|\mathbf{\Psi}_n\right\rangle \\ \left\langle\mathbf{\Gamma}_n\right| \hat{H}_\tau = \omega_n{}' \left\langle\mathbf{\Gamma}_n\right| \end{cases}. \tag{S76}$$

The first equation is a rewrite of Eq. (S42). If the energy is non-degenerate and $|\Psi\rangle$ and $\langle\Gamma|$ form an exact biorthogonal set, we have:

$$\begin{cases} \omega_n = \omega_n{}' \\ \left\langle\mathbf{\Gamma}_n \middle| \mathbf{\Psi}_m\right\rangle = 0, \ n \neq m. \end{cases} \tag{S77}$$

For our system with boundary coupling strength τ, the Hamiltonian can be expressed as the sum of the OBC Hamiltonian and its perturbation part

$$\hat{H}_\tau = \hat{H}_0 + \tau \hat{H}_{\text{pert}} . \tag{S78}$$

The Hamiltonian $\widehat{H}_0$ has the same form as Eq. (S30). To avoid confusion, we use $\omega_n^{(0)}$, $\left|\Psi_n^{(0)}\right\rangle$, and $\left\langle\Gamma_n^{(0)}\right|$ to represent the eigenvalues, right eigenvector, and left eigenvector of $\widehat{H}_0$, respectively. This means:

$$\begin{cases} \hat{H}_0 \left|\mathbf{\Psi}_n^{(0)}\right\rangle = \omega_n^{(0)} \left|\mathbf{\Psi}_n^{(0)}\right\rangle \\ \left\langle\mathbf{\Gamma}_n^{(0)}\right| \hat{H}_0 = \omega_n^{(0)} \left\langle\mathbf{\Gamma}_n^{(0)}\right|. \end{cases} \tag{S79}$$

Then, $\widehat{H}_{\text{pert}}$ can be simply derived from Eqs. (S30) and (S41):

$$\begin{aligned} \hat{H}_{\text{pert}} &= i \begin{bmatrix} -1 & 0 & \cdots & 0 & 1 \\ 0 & 0 & \cdots & 0 & 0 \\ \vdots & \vdots & \ddots & \vdots & \vdots \\ 0 & 0 & \cdots & 0 & 0 \\ 1 & 0 & \cdots & 0 & -1 \end{bmatrix}_{N\times N} \\ &= -i\left(\hat{c}_1^\dagger \hat{c}_1 + \hat{c}_N^\dagger \hat{c}_N\right) + i\left(\hat{c}_1^\dagger \hat{c}_N + \hat{c}_N^\dagger \hat{c}_1\right). \end{aligned} \tag{S80}$$

The eigenvalues and right eigenvectors of $\widehat{H}_\tau$ can be expanded by[2]:

$$\left|\mathbf{\Psi}_n\right\rangle = \left|\mathbf{\Psi}_n^{(0)}\right\rangle + \tau \left|\mathbf{\Psi}_n^{(1)}\right\rangle + \tau^2 \left|\mathbf{\Psi}_n^{(2)}\right\rangle + \cdots \tag{S81}$$

$$\omega_n = \omega_n^{(0)} + \tau\omega_n^{(1)} + \tau^2\omega_n^{(2)} + \cdots. \tag{S82}$$

Here, the superscripts (i), $i = 1,2,3,$ ..., denote the i-th order correction term. By operating Eq. (S81) on Eq. (S78), along with Eq. (S82), we can extract the equation concerning the first-order term of τ:

$$\tau\left(\omega_n^{(0)} - \hat{H}_0\right)\left|\boldsymbol{\Psi}_n^{(1)}\right\rangle + \tau\omega_n^{(1)}\left|\boldsymbol{\Psi}_n^{(0)}\right\rangle = \tau\hat{H}_{\text{pert}}\left|\boldsymbol{\Psi}_n^{(0)}\right\rangle. \tag{S83}$$

By operating $\left\langle\Gamma_m^{(0)}\right|$ on Eq. (S83), and based on the relations in Eq. (S77), we obtain:

$$\tau\left(\omega_n^{(0)} - \omega_m^{(0)}\right)\left\langle\boldsymbol{\Gamma}_m^{(0)}\middle|\boldsymbol{\Psi}_n^{(1)}\right\rangle + \tau\omega_n^{(1)}\left\langle\boldsymbol{\Gamma}_m^{(0)}\middle|\boldsymbol{\Psi}_n^{(0)}\right\rangle = \left\langle\boldsymbol{\Gamma}_m^{(0)}\middle|\tau\hat{H}_{\text{pert}}\middle|\boldsymbol{\Psi}_n^{(0)}\right\rangle. \tag{S84}$$

When $n = m$, the first-order non-Hermitian perturbation theory can be derived as:

$$\tau\omega_n^{(1)} = \frac{\left\langle\boldsymbol{\Gamma}_n^{(0)}\middle|\tau\hat{H}_{\text{pert}}\middle|\boldsymbol{\Psi}_n^{(0)}\right\rangle}{\left\langle\boldsymbol{\Gamma}_n^{(0)}\middle|\boldsymbol{\Psi}_n^{(0)}\right\rangle} \approx \omega_n - \omega_n^{(0)} = \Delta\omega_n. \tag{S85}$$

Therefore, as long as we know the energy shift of a certain eigenvalue, we can use the left and right eigenvectors in the OBC to determine the boundary coupling strength τ. The condition for the validity of Eq. (S85) is that the boundary coupling strength must be small, meaning no phase change (energy degeneracy) occurs during perturbation.

For the OBC case, we choose the symmetric point ($\frac{N}{2}$-th eigenvalue) as our perturbation point. Substituting the eigenvectors in Eqs. (S64) and (S65) into Eq. (S85), we can derive Eq. (6) in the main text:

$$\Delta\omega_{N/2} = \frac{2i\tau\left[\left(-r^2\right)^{N/2} - \left(-r^{-2}\right)^{N/2-1} - r^2 - 1\right]}{N\left(1+r^2\right)}, \tag{S86}$$

where $r = \sqrt{h_+/h_-}$ has the same definition as in Eq. (S52). When the site number N is large, Eq. (S86) can be simplified to $\Delta\omega_{N/2} \approx (-1)^{N/2}[2i/(1+r^2)]e^{N\ln r - \ln N}\tau$. Since r can be treated as a fixed number once the non-reciprocal strength is determined, the site number N can exponentially influence the test sensitivity of this system. The testing sensitivity is defined as $S = \left|\Delta\omega_{N/2}/\tau\right|$, indicating the amplification factor of the boundary coupling strength on the $\frac{N}{2}$-th energy shift.

Substituting Eq. (S33) into the expression of sensitivity, we have:

$$S = \left| \frac{2i}{N} \left[(-1)^{N/2} \frac{\cosh\left(\frac{vL_{\text{pipe}}(N-1)}{2\alpha} \right)}{\cosh\left(\frac{vL_{\text{pipe}}}{2\alpha} \right)} - 1 \right] \right|. \tag{S87}$$

When the parameters N and v are sufficiently large, the above expression can be approximated as:

$$S \approx \frac{2}{N} e^{\frac{|v|L_{\text{pipe}}(N-2)}{2\alpha}} = \frac{2}{N} e^{(N-2)|g|}. \tag{S88}$$

It is observed that the sensitivity will have a near exponential growth with the increase of both the site number N and the imaginary gauge potential g (or the advective velocity v). This near-exponential growth of the sensitivity S is a direct manifestation of the directional pumping mechanism induced by the synthetic imaginary gauge field g. This phenomenon is universal. Physically, the non-reciprocal lattice can be envisioned as a high-gain directional amplifier chain, where each additional site N represents an incremental stage along the exponential amplification path. While the dynamic range $\tau_{\max}$ is determined by the threshold at which boundary feedback triggers a spectral collapse, the sensitivity S reflects the total integrated gain of a "pumped" boundary signal as it traverses the lattice. The imaginary gauge potential g (linearly dependent on the advective velocity v) determines the gain per stage, while the site number N defines the total length of the amplification path. Due to the NHSE, the spatial separation of the biorthogonal left and right eigenstates ensures that a boundary perturbation τ is "swept" across the entire lattice by the directional flow, accumulating a massive response factor of $e^{N|g|}$. This mechanism allows infinitesimal perturbations to be accumulated into macroscopic frequency shifts, providing a sensing performance several orders of magnitude higher than that of conventional reciprocal diffusive systems.

Fig. S5a illustrates the phase diagram of $\log_{10} S$, which exhibits a clear transition across the parameter space. A "Phase Change Line" is identified, separating the regime of linear response from the regime where the NHSE dominates, leading to a significant enhancement of the eigenmode shift. As further demonstrated in Fig. S5b, the sensitivity grows exponentially with the convection velocity v. The analytical solution Eq. (S87) (solid blue line) is in agreement with the asymptotic approximation Eq. (S88) (dashed grey line),

especially in the high-velocity regime. This near exponential scaling serves as a hallmark of NHSE-enhanced sensing, providing several orders of magnitude higher sensitivity compared to conventional reciprocal diffusive systems.

We next numerically plot the logarithm of S as a function of the site number N and the logarithm of τ in Fig. S6. When a phase transition occurs, the energy shift is drastic, resulting in a discontinuous upheaval of S. Therefore, a singular line appears in this plot, representing the phase-transition threshold of this system. The grey dashed line represents our analytical result calculated from Eq. (S70). The phase-transition line aligns perfectly with the discontinuous upheaval, demonstrating the consistency between our numerical and analytical results. We capture two fixed τ lines in the color map (blue and pink dashed lines) and replot their sensitivity-site number relationship in Fig. S6(I). For $\tau = 10^{-8}$ (blue dashed line), the scatter plot is approximately linear in the larger N, reflecting the fact that N can exponentially influence the sensitivity S. Throughout this region, the parameters remain below the phase-transition line, so perturbation theory stays valid. For $\tau = 10^{-4}$ (pink dashed line), the lattice can contain at most 16 sites (marked by a pink pentagon); any larger N would cross the phase-transition line.

We then extracted data along two fixed N lines from the color map (represented by the blue and pink solid lines) and replotted their sensitivity-coupling (τ) relationships in Fig. S6(II). When the coupling strength τ is lower than the phase transition threshold, the sensitivity remains constant for each configuration. However, once the coupling term exceeds this threshold, the sensitivity undergoes a drastic upheaval, as indicated by the two five-pointed stars in the plot. Consequently, our sensing system can operate in two distinct modes: (1) Quantitative sensing: utilizing the stable regime below the phase transition line for precise thermal coupling measurements. (2) Qualitative detection: leveraging the abrupt phase change to determine whether the test sample exceeds the critical coupling threshold $\tau_{\max}$.

Notably, by multiplying Eq. (S75) and Eq. (S88), we have:

$$\tilde{\tau}_{\max} S \approx \frac{2g}{N \sinh(g)}. \tag{S89}$$

This equation indicates that the product of dynamic range and sensitivity must cancel the exponential dual scaling terms $e^{\pm|g|(N-2)}$, indicating a fundamental trade-off in non-Hermitian sensing systems.

To verify the analytical predictions of the dual scaling law for the $N/2$-th state in the Hatano-Nelson model, we performed comprehensive numerical analyses, with the results presented in Fig. S7. Fig. S7(a, d) and (b, e) illustrate the evolution of the perturbative sensitivity S and the dynamic range $\tau_{\max}$ with respect to the lattice size N and the synthetic imaginary gauge field g, respectively. The results clearly demonstrate that both quantities exhibit strong exponential dependencies: the exponential sensitivity gain induced by the non-reciprocal pumping ($S \propto e^{|g|N}$) is inevitably accompanied by an exponential contraction of the dynamic range ($\tau_{\max} \propto e^{-|g|N}$).

Crucially, the product of sensitivity and dynamic range ($S \cdot \tau_{\max}$) directly defines the performance boundary of the sensing system. According to Eq. (S89), this product depends on the effective hopping strength h_{eff}. While the effective hopping strength is typically a system constant, in our advection-induced non-reciprocal system, h_{eff} can be tuned via the g (Eq. (S36)). Given that g remains bounded in physical systems, the product approaches a constant value in the small g regime, as illustrated by the nearly horizontal plateau in Fig. S7f. Furthermore, Fig. S7c reveals that the product exhibits an algebraic $1/N$ decay characteristic with respect to N. This phenomenon profoundly reflects the finite-size quantization effect of the bulk energy level spacing in a one-dimensional lattice: in the bulk spectrum, the triggering threshold for the exceptional point degeneracy is strictly bounded by the energy spacing of adjacent quantized levels. The high degree of agreement between the numerical results (blue dots) and the asymptotic analytical solutions (red dashed lines) across the parameter space further corroborates the robustness of our theoretical framework.

According to the Bauer-Fike theorem, the condition numbers of non-normal matrices can be exceptionally large, leading to significant divergence between the pseudospectrum and the spectrum, even under infinitesimal perturbations. As sensitivity is enhanced by increasing the site number N or the non-reciprocal coupling strength, the system becomes increasingly ill-conditioned and unstable. Fig. S8

illustrates the condition numbers and their exponential growth as a function of N and v. Such instability triggers an exponential contraction of the dynamic range, providing lateral evidence for the fundamental trade-off between enhanced sensitivity and the inevitable reduction of the linear operational regime.

Supplementary Note 5: The Universal Dual Scaling Law and the Fundamental Sensing Trade-off for Su-Schrieffer-Heeger Model

For a Su-Schrieffer-Heeger (SSH) model, where N is an odd number to ensure the emergence of the zero-energy mode:

$$H_{\mathrm{SSH}}=\begin{bmatrix} 0 & h_- & 0 & 0 & 0 & \cdots & \tau \\ h_+ & 0 & t_2 & 0 & 0 & \cdots & 0 \\ 0 & t_2 & 0 & h_- & 0 & \cdots & 0 \\ 0 & 0 & h_+ & 0 & \ddots & \cdots & 0 \\ 0 & 0 & 0 & \ddots & \ddots & h_- & 0 \\ \vdots & \vdots & \vdots & \ddots & h_+ & 0 & t_2 \\ \tau & 0 & 0 & 0 & 0 & t_2 & 0 \end{bmatrix}_{N\times N}. \tag{S90}$$

The bulk equations for Eq. (S90) are:

$$\begin{aligned} h_+\psi_{s,A}+t_2\psi_{s+1,A}&=E\psi_{s,B} \\ t_2\psi_{s-1,B}+h_-\psi_{s,B}&=E\psi_{s,A} \end{aligned}. \tag{S91}$$

By substituting the Bloch solutions:

$$\begin{aligned} \psi_{s,A}&=z^s\phi_A \\ \psi_{s,B}&=z^s\phi_B \end{aligned}, \tag{S92}$$

the secular equation can be obtained as:

$$E^2=\left(h_++t_2z\right)\left(h_-+t_2z^{-1}\right). \tag{S93}$$

The amplitude relations are given by:

$$\frac{\phi_A}{\phi_B} = \frac{E}{h_+ + t_2 z}$$
$$\frac{\phi_A}{\phi_B} = \frac{h_- + t_2 z^{-1}}{E} \quad . \tag{S94}$$

According to Vieta's formulas:

$$z_1 z_2 = \frac{h_+}{h_-} = r^2 \quad , \tag{S95}$$

Thus, Eq. (S94) can be rewritten as:

$$\begin{aligned} \phi_B^{(1)} &= \frac{h_+ + t_2 z_1}{E} \phi_A^{(1)} = \gamma\left(z_1\right) \phi_A^{(1)} = \gamma_1 \phi_A^{(1)} \\ \phi_B^{(2)} &= \frac{h_+ + t_2 z_2}{E} \phi_A^{(2)} = \gamma\left(z_2\right) \phi_A^{(2)} = \gamma_2 \phi_A^{(2)}. \end{aligned} \tag{S96}$$

The general solution for the wave function is:

$$\psi_s = c_1 {z_1}^s + c_2 {z_2}^s \quad . \tag{S97}$$

Assuming $M = \frac{N+1}{2}$, the boundary equations are:

$$\begin{aligned} h_- \psi_{1,B} + \tau \psi_{M,A} &= E \psi_{1,A} \\ t_2 \psi_{M-1,B} + \tau \psi_{1,A} &= E \psi_{M,A}. \end{aligned} \tag{S98}$$

Combining the bulk and boundary equations yields:

$$\begin{aligned} \tau \psi_{M,A} - t_2 \psi_{0,B} &= 0 \\ \tau \psi_{1,A} - h_- \psi_{M,B} &= 0. \end{aligned} \tag{S99}$$

Substituting the Bloch solutions (S97) and expanding with $(c_1, c_2)^T$ as the basis gives:

$$H_{\mathrm{B}} = \begin{bmatrix} \tau {z_1}^M \phi_A^{(1)} - t_2 {z_1}^0 \phi_B^{(1)} & \tau {z_2}^M \phi_A^{(2)} - t_2 {z_2}^0 \phi_B^{(2)} \\ \tau {z_1}^1 \phi_A^{(1)} - h_- {z_1}^M \phi_B^{(1)} & \tau {z_2}^1 \phi_A^{(2)} - h_- {z_2}^M \phi_B^{(2)} \end{bmatrix}. \tag{S100}$$

Substituting Eq. (S96) into Eq. (S100) yields:

$$H_{\mathrm{B}}=\begin{bmatrix}\tau z_1^{M}\phi_A^{(1)}-t_2 z_1^{0}\gamma\left(z_1\right)\phi_A^{(1)} & \tau z_2^{M}\phi_A^{(2)}-t_2 z_2^{0}\gamma\left(z_2\right)\phi_A^{(2)}\\ \tau z_1^{1}\phi_A^{(1)}-h_{-} z_1^{M}\gamma\left(z_1\right)\phi_A^{(1)} & \tau z_2^{1}\phi_A^{(2)}-h_{-} z_2^{M}\gamma\left(z_2\right)\phi_A^{(2)}\end{bmatrix}$$
$$=\begin{bmatrix}\tau z_1^{M}-t_2\gamma\left(z_1\right) & \tau z_2^{M}-t_2\gamma\left(z_2\right)\\ \tau z_1-h_{-} z_1^{M}\gamma\left(z_1\right) & \tau z_2-h_{-} z_2^{M}\gamma\left(z_2\right)\end{bmatrix}\begin{bmatrix}\phi_A^{(1)} & \\ & \phi_A^{(2)}\end{bmatrix}. \tag{S101}$$

For $(c_1, c_2)^T$ to have non-trivial solutions, the determinant of the above matrix must be zero:

$$\tau^2(z_1^M z_2 - z_2^M z_1) - \tau h_{-}(z_1 z_2)^M(\gamma_2-\gamma_1) - \tau t_2(\gamma_1 z_2 - \gamma_2 z_1) + t_2 h_{-}\gamma_1\gamma_2(z_2^M - z_1^M) = 0. \tag{S102}$$

Using Eqs. (S94), (S95), and (S96), the aforementioned boundary equation can be further rigorously simplified to:

$$\frac{\tau t_2}{E}\left[\left(r^2\right)^{M-1}+1\right] = t_2\frac{z_1^M - z_2^M}{z_1 - z_2} - \frac{\tau^2}{h_{-}}\frac{z_1^{M-1} - z_2^{M-1}}{z_1 - z_2}. \tag{S103}$$

From Eq. (S95), we obtain:

$$\begin{aligned} z_1 &= re^{i\theta}\\ z_2 &= re^{-i\theta}. \end{aligned} \tag{S104}$$

Substituting this into Eq. (S103) and expanding via Euler's formula yields:

$$\sin(M\theta) - \frac{\tau^2}{t_1 t_2}\sin[(M-1)\theta] = \frac{\tau}{E}\left[r^{M-1} + r^{-(M-1)}\right]\sin\theta. \tag{S105}$$

Here, we parameterize the non-reciprocal hopping in the form of a synthetic imaginary gauge field:

$$\begin{aligned} h_{+} &= t_1 e^{g}\\ h_{-} &= t_1 e^{-g}, \end{aligned} \tag{S106}$$

where t_1 is the base hopping term and g is the imaginary gauge potential. Recalling Eq. (S93), the precise expression for E can be similarly determined as:

$$E = \pm\sqrt{t_1^2 + t_2^2 + 2t_1 t_2\cos\theta}. \tag{S107}$$

To analytically characterize the topological zero-energy mode localized at the system boundary, we must perform an analytic continuation of the real wave vector θ in the bulk equations (Eq. (S104)) into the complex plane. For an exponentially decaying edge state, we introduce the complex wave vector ansatz:

$$\theta = \pi + i\varphi, \tag{S108}$$

where $\varphi > 0$ represents the decay constant of the edge state. Expanding this via Euler's formula yields $\sin(\pi + i\varphi) = -i\sinh(\varphi)$ and $\cos(\pi + i\varphi) = -\cosh(\varphi)$. Substituting this complex wave vector into the dispersion relation (Eq. (S107)), the exact energy evolution of the topological edge state is rewritten as:

$$E(\varphi) = \pm\sqrt{t_1^2 + t_2^2 - 2t_1 t_2 \cosh(\varphi)}. \tag{S109}$$

Furthermore, substituting this into the bulk transcendental equation (Eq. (S105)) and incorporating the synthetic imaginary gauge field parameter defined in Eq. (S106), the trigonometric equation governing extended states is strictly transformed into a hyperbolic secular equation dedicated to the topological edge state:

$$\sinh(M\varphi) + \frac{\tau^2}{t_1 t_2}\sinh[(M-1)\varphi] = \frac{\tau}{|E|}\left[e^{g(M-1)} + e^{-g(M-1)}\right]\sinh(\varphi). \tag{S110}$$

As the boundary perturbation τ gradually increases, the edge state shifts towards the bulk band. At the topological phase transition critical point (the Exceptional Point), the edge state completely loses its localization and merges with the continuous bulk states, which corresponds to the limit $\varphi \to 0$. In the limit of $\varphi \to 0$, the system energy $|E|$ approaches the edge of the bulk band gap:

$$\lim_{\varphi \to 0} |E(\varphi)| \approx |t_1 - t_2| \equiv E_c, \tag{S111}$$

where E_c is the intrinsic bulk band gap protected by the system parameters. Concurrently, applying the first-order Taylor expansion $\sinh(x)|_{x\to 0} \approx x$ to the hyperbolic secular equation and factoring out the common term φ, we obtain the algebraic equation for the phase transition perturbation $\tau_{\max}$:

$$E_c\left[M + \frac{\tau_{\max}^2}{t_1 t_2}(M-1)\right] = \tau_{\max}\left[e^{g(M-1)} + e^{-g(M-1)}\right]. \tag{S112}$$

Since we are focusing on the perturbative response regime, $(\tau_{\max})^2$ is a negligibly small higher-order term. Neglecting this term directly yields the universal scaling law for the maximum linear dynamic range of the non-reciprocal sensing system:

$$\tau_{\max} \approx \frac{ME_c}{e^{g(M-1)} + e^{-g(M-1)}}. \tag{S113}$$

This analytical result profoundly reveals that in the presence of a synthetic gauge field, the maximum detectable perturbation range undergoes a severe exponential decay as the lattice size M and/or gauge field $|g|$ increase.

$$\tau_{\max} \propto ME_c e^{-|g|(M-1)}. \tag{S114}$$

We can define the base hopping ratio as:

$$\rho = \frac{t_1}{t_2}. \tag{S115}$$

When $\rho < 1$, the system operates in the topologically non-trivial phase of the SSH model. The intrinsic bulk band gap can be approximated as $E_c = t_2 - t_1 = t_2(1-\rho)$. The perturbative sensitivity of the SSH model is derived as[3]:

$$S = \left|\frac{\Delta\omega}{\tau}\right| = \left|\frac{\left(\rho^2 - 1\right)\left[\left(-\rho r^{-1}\right)^{M-1} + \left(-\rho r\right)^{M-1}\right]}{\rho^{2M} - 1}\right|. \tag{S116}$$

In the large-M limit, Eq. (S116) can be simplified to:

$$S \approx \left(1-\rho^2\right)\left[\rho \cdot e^{|g|}\right]^{M-1} = \left(1-\rho^2\right)e^{(-|\ln\rho|+|g|)(M-1)}. \tag{S117}$$

As evidenced by Eqs. (S113) and (S117), the system adheres to the dual scaling law: both sensitivity and dynamic range exhibit an exponential dependence on the number of cells M and the gauge potential $|g|$. Notably, the exponential factor $-|\ln\rho| + |g|$ in Eq. (S117) fundamentally elucidates the physical mechanism underlying the sensitivity amplification. It arises from the competition between the topological localization effect (characterized by $|\ln\rho|$, which tends to confine the wave function at the boundary) and the non-Hermitian skin effect (characterized by $|g|$, which provides a unidirectional probability flow). Only when the skin effect overcomes the topological localization (i.e., $|g| > |\ln\rho|$) does the sensitivity experience an exponential growth with respect to the system size M.

The product of these two quantities defines the sensitivity-dynamic range product, given by:

$$S \cdot \tau_{\max} \approx E_c \left(1-\rho^2\right) M e^{-|\ln \rho|(M-1)} . \quad \text{(S118)}$$

Eq. (S118) unveils the relationship between the perturbative sensitivity and the dynamic range. Remarkably, the dual scaling terms $e^{\pm|g|(M-1)}$ completely vanish from this product, underscoring a fundamental trade-off governed only by the intrinsic static properties of the lattice.

To rigorously validate the dual scaling law for the topological zero-mode, we performed numerical eigenvalue analyses on the non-Hermitian SSH model under varying lattice sizes N and gauge field strengths g. As depicted in Fig. S9(a, d) and (b, e), both the perturbative sensitivity S and the dynamic range $\tau_{\max}$ exhibit quintessential exponential scaling behaviors.

Crucially, the behavior of the sensitivity-dynamic range product ($S \times \tau_{\max}$) decouples the macroscopic non-Hermitian pumping from the intrinsic band features. As demonstrated in Fig. S9f, the product remains invariant across varying imaginary gauge field strengths g. This invariant horizontal plateau provides definitive numerical proof of the exact mathematical cancellation of the non-Hermitian exponential skin-effect factors. Conversely, with respect to the lattice size, Fig. S9c reveals that the product is not a constant, but rather exhibits an intrinsic decay governed by the scaling factor. According to Eq. (S118), the product diminishes as M increases, with the rate of decay determined by $|\ln \rho|$. Specifically, while a larger ρ widens the bandgap and enhances the dynamic range, it simultaneously strengthens topological localization. This localization competes with the non-Hermitian skin effect, ultimately compromising the sensitivity. Consequently, optimizing non-Hermitian sensing within the SSH framework requires a meticulous balancing of these competing factors to achieve peak performance.

Beyond the rigorous finite-size scaling analysis (Eq. (S118)), this fundamental trade-off can be understood intuitively. In a topological sensing platform, the operational regime is strictly bounded by the intrinsic bulk band gap $E_c = t_2 - t_1$. This gap acts as a rigid "energy ceiling"; once the perturbation-induced energy shift of the zero-mode reaches this threshold, the highly localized edge state delocalizes, hybridizes with the continuous bulk modes, and the topological protection is utterly destroyed. The

perturbative sensitivity S dictates the initial linear rate at which the eigenenergy climbs towards this ceiling. If we define the effective linear dynamic range, $\tau_{\max}^{\mathrm{lin}}$, as the maximum perturbation the system can endure while maintaining this constant linear response until it strikes the bulk band edge, the relationship geometrically simplifies to $S \cdot \tau_{\max}^{\mathrm{lin}} = E_c = t_2 - t_1$.

It is worth noting that the above calculations are fundamentally asymptotic approximations, designed to capture the dominant exponential scaling behavior of the system rather than a strict algebraic equality at all scales. In a rigorous sense, two subtle approximations are embedded in this analytical framework. First, owing to the finite-size effect, the topological phase transition (i.e., the exceptional point) occurs when the edge mode merges with the nearest discrete, quantized bulk energy level, which does not perfectly align with the thermodynamic continuous bulk band edge E_c. Second, the perturbative sensitivity S and the dynamic range $\tau_{\max}$ are derived by expanding the secular equation around two distinct physical limits: the highly localized zero-energy limit ($\varphi \to \varphi_0$) and the delocalized EP limit ($\varphi \to 0$), respectively. Nevertheless, bridging these two limits to extract their product provides a highly effective scaling estimation. It intuitively elucidates the underlying physical trend: any exponential gain in sensitivity is inevitably and universally counterbalanced by an exponential loss in dynamic range, dictating the fundamental sensing trade-off.

Supplementary Note 6: Experimental Analysis

The robustness analysis consists of several parts. Here, we take the system with $N = 6$, $v = 0.2\ \mathrm{mm\ s^{-1}}$ under open boundary condition as an example to evaluate the robustness of our thermal coupling sensing system.

First, to evaluate the impact of potential inconsistencies in the thermal excitation process, we examined the system's spectral response under varying heating conditions. Given that the system spectrum is derived from sequential heating of individual cavities, fluctuations in the performance of heating elements or variations in temperature rise times could introduce errors. To quantify this effect, we conducted experiments under two distinct heating voltages (12 V and 14 V), effectively modulating the temperature

rise rates to evaluate the system's response. As shown in Fig. S10a, the resulting spectral shifts remain within a narrow error margin. This high degree of consistency demonstrates that the system is insensitive to variations in heating efficiency.

Second, we considered errors due to background temperature variation. Since background temperature must be subtracted before processing raw data, we tested different subtraction values from 24.5 °C to 25.5 °C (the actual background temperature is 25 °C). The resulting eigenvalue shifts are shown as error bars in Fig. S10b. Misestimation of background temperature significantly affects eigenvalues with large mode indices, which correspond to slower decay rates. Slow-decay eigenvalues are more sensitive to background temperature inaccuracies, and in extreme cases, improper subtraction may even lead to negative temperatures, affecting matrix diagonalization and eigenvalue fitting. However, since we focus on the $N/2$-th eigenvalue, which has a relatively high decay rate, the effect of background temperature misestimation is limited.

Third, we analyzed the primary noise sources within our testing system, specifically focusing on the noise originating from the transient temperature detection by the thermal infrared camera. To identify the main noise characteristics, we measured the temperature of a constant-temperature sample over a duration of 416 seconds. The results are presented in a quantile-quantile (Q-Q) plot with a standard Gaussian reference in Fig. S11a. The error distribution closely approximates a Gaussian distribution. To quantify this, we replotted the experimental data in the histogram shown in Fig. S11b and fitted it to a Gaussian profile, thereby determining the mean and standard deviation of the system's measurement noise.

We subsequently added Gaussian noise of this magnitude back into our transient data to observe the resulting relative error, shown in Fig. 4c, main text. The results demonstrate a significant difference: the LOWESS method effectively assists in recovering frequency-domain eigenvalues from transient data and enhances the robustness of this recovery against Gaussian noise.

In Fig. S12, we further demonstrate the process of fitting transient data to eigenvalues. Fig. S12a shows a fitting curve where the raw data (without LOWESS) exhibited small-scale fluctuations, leading to a relatively high fitting error. In contrast, the case utilizing LOWESS (Fig. S12b) results in smoother data

with significantly reduced fluctuations. Consequently, the relative fitting error is minimized. Ultimately, the LOWESS method effectively denoises and smoothes the raw data, yielding a more accurate and reliable spectrum.

One apparent contradiction is how a highly sensitive measurement system can also be robust to noise. The reason lies in the fact that our system's extreme sensitivity originates from the NHSE, which leads to exponential amplification of the bra and ket wavefunctions at opposite boundaries. As a result, the influence of the test sample—which couples the two boundaries—is significantly enhanced. In contrast, noise does not act as a coupling mechanism, but rather introduces inaccuracies that are not amplified in the same way. Therefore, the effect of noise remains relatively small. However, as shown in the pseudospectrum in Fig. 4f, larger non-Hermitian systems may exhibit greater instability. This indicates that noise interference remains an important consideration when designing large-scale non-Hermitian systems.

References

1. Li, Y. & Li, J. Advection and thermal diode. *Chinese Phys. Lett.* **38**, 030501 (2021).
2. Brody, D. C. Biorthogonal quantum mechanics. *J. Phys. A: Math. Theor.* **47**, 035305 (2014).
3. Budich, J. C. & Bergholtz, E. J. Non-Hermitian Topological Sensors. *Phys. Rev. Lett.* **125**, 180403 (2020).

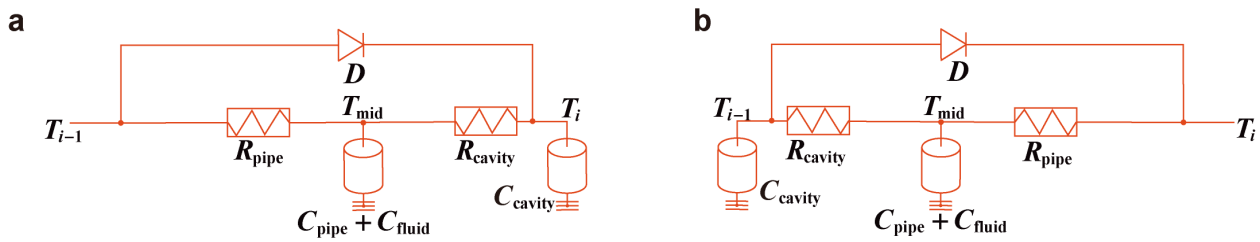

670

671 **Fig. S1 | Thermal circuit equivalence under different viewing directions. a,** Distributed thermal circuit
672 viewed along the flow direction (left to right). **b,** Distributed thermal circuit viewed against the flow
673 direction (right to left).

674

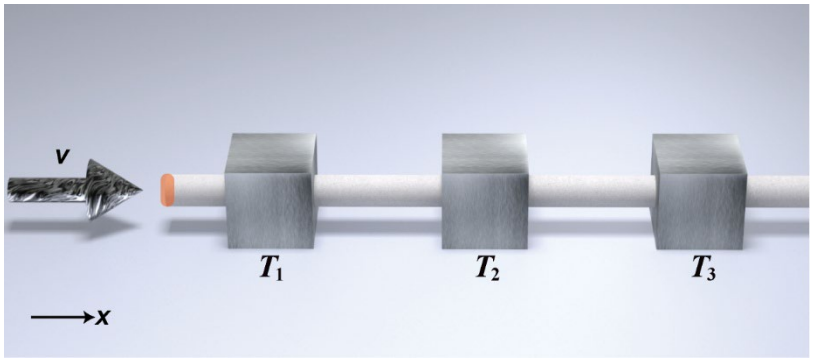

675

676 **Fig. S2 | Layout of the first three cavities.** Liquid metal flows at velocity v along $+x$ direction. Cavity

677 temperatures are denoted by T_1, T_2, and T_3. Orange shading marks the input boundary.

678

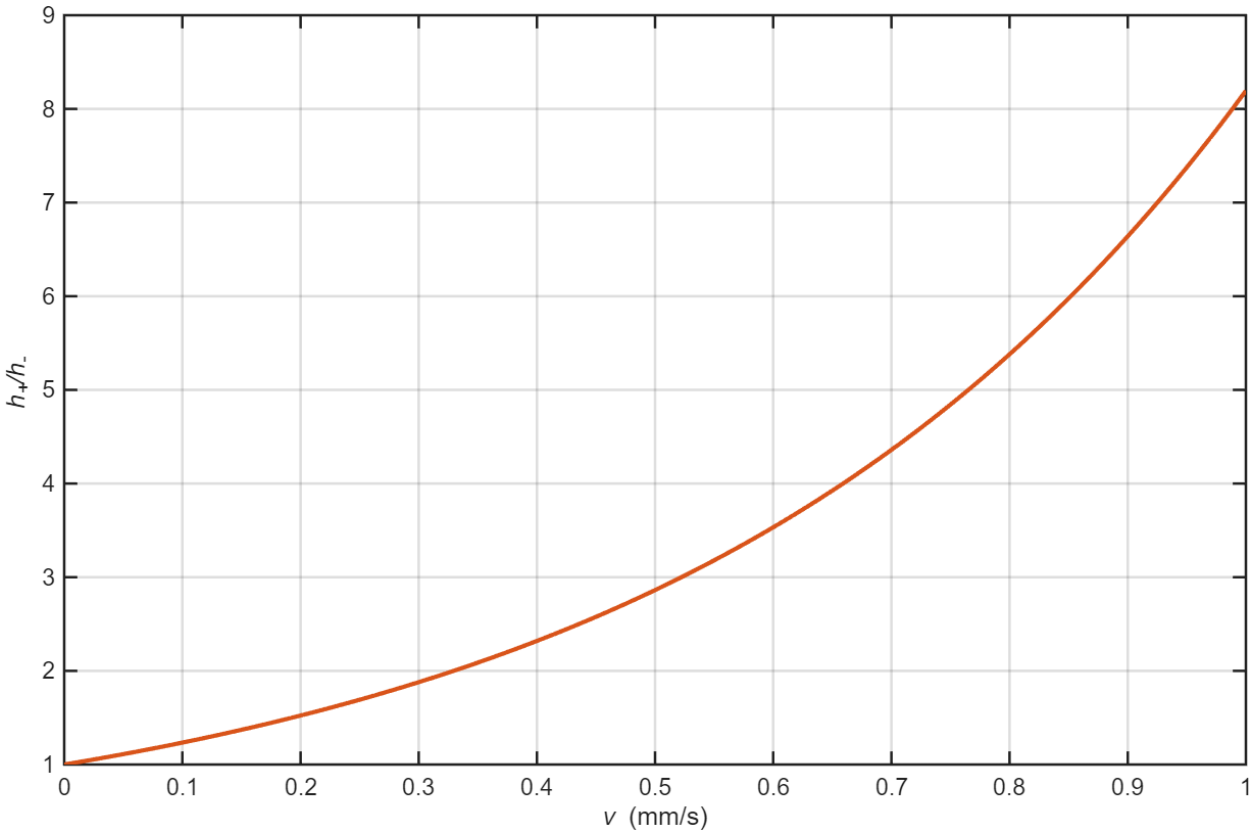

Fig. S3 | Tuning the coupling asymmetry via flow velocity. Evolution of the non-reciprocal ratio h_+/h_- relative to the liquid-metal flow velocity. The curve highlights the transition from reciprocal transport (h_+/h_- at $v = 0$) to strongly non-reciprocal regimes as the flow velocity increases. This rapid growth in coupling asymmetry underpins the extreme sensitivity of the non-Hermitian thermal sensor, enabling a broad dynamic range for boundary perturbation sensing.

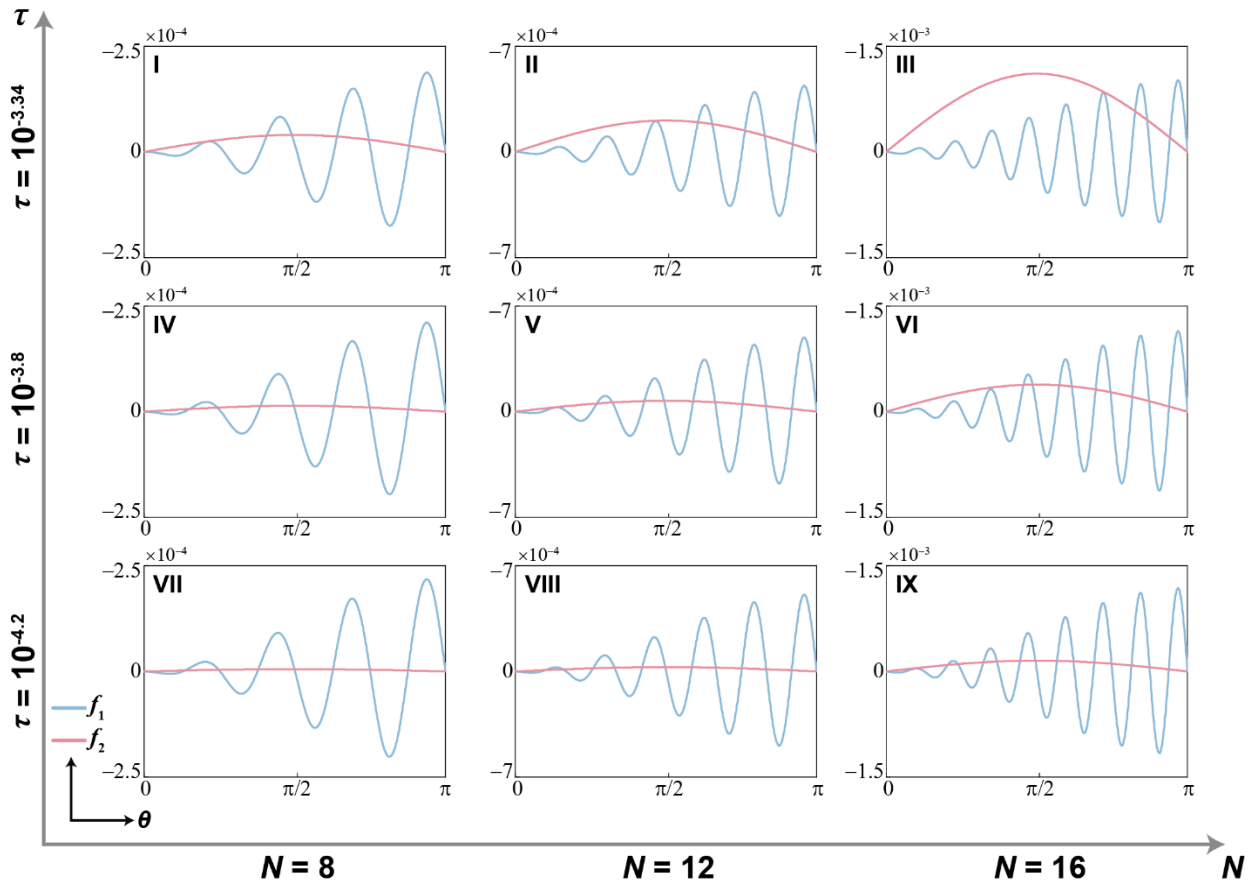

Fig. S4 | Phase transition behaviour via intersection analysis. Functions f_1 and f_2 are plotted versus θ for varying site number N and boundary coupling strengths τ. The number of intersections corresponds to the number of pure imaginary solutions in the spectrum.

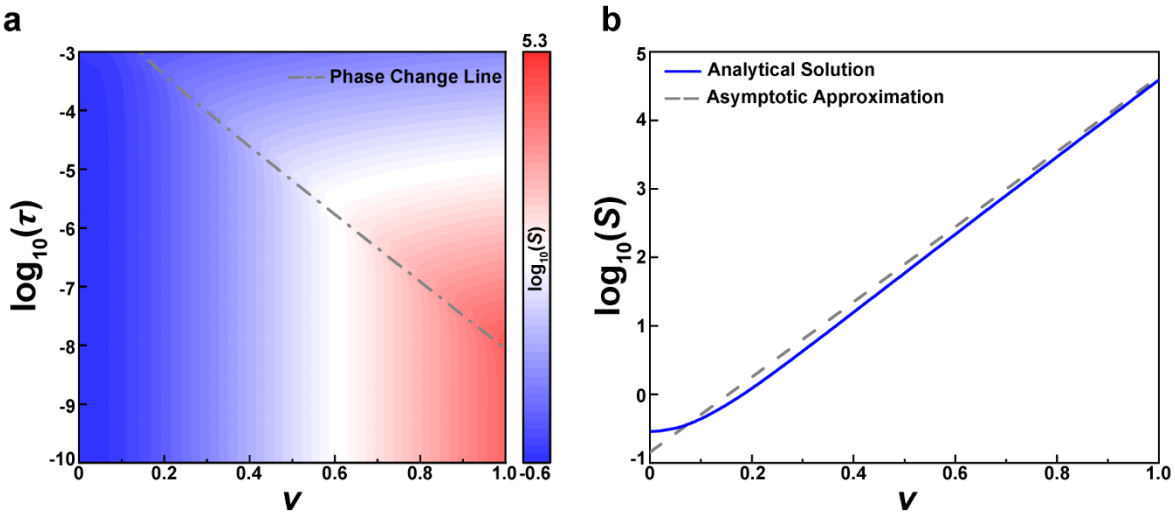

Fig. S5 | Sensitivity analysis as a function of advective velocity under $N = 14$. a, Phase diagram of the sensing sensitivity as a function of the velocity v and the perturbation coupling strength $\log_{10}\tau$. The dashed line indicates the analytical phase change boundary, highlighting the transition from linear regime to non-linear (degenerate) regime. **b,** Comparison between the analytical solution and the asymptotic exponential approximation for the sensitivity versus convection velocity. The logarithmic scale on the y-axis demonstrates the nearly exponential amplification characteristic of the NHSE.

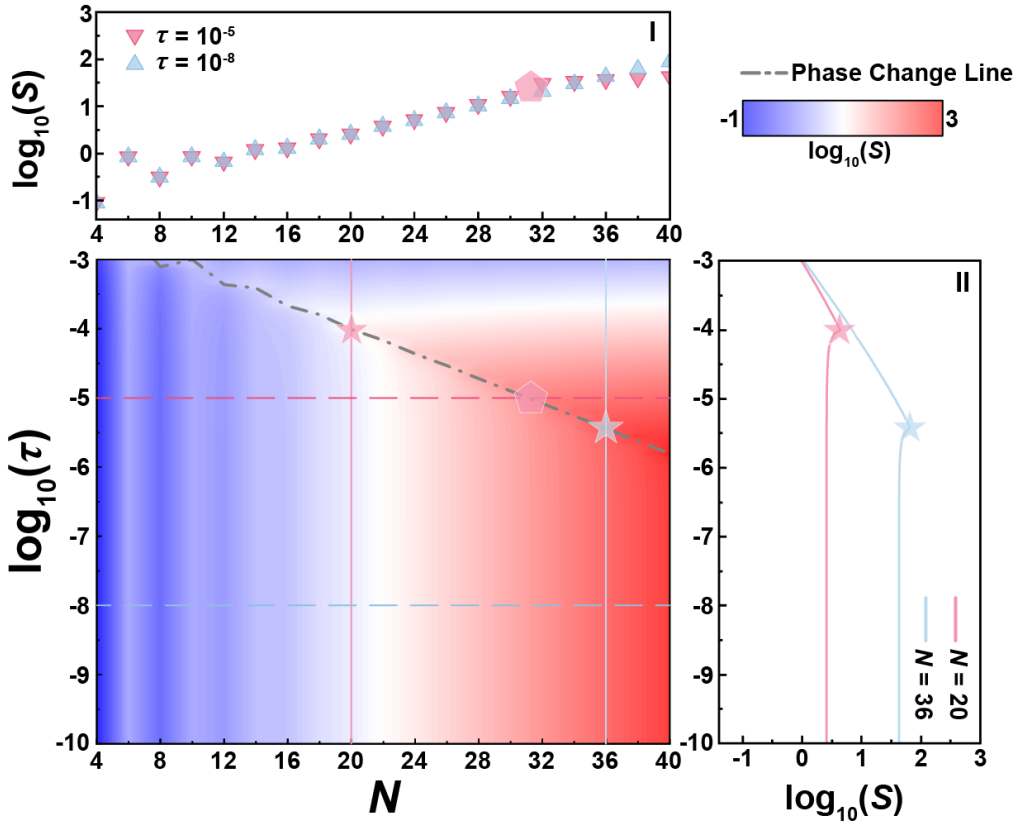

Fig. S6 | Testing sensitivity with varied τ and N. The color map displays the logarithm of sensing sensitivity as a function of boundary coupling strength τ and site number N. The grey dash-dot line indicates the theoretical phase transition threshold of the system, which aligns with abrupt changes in the sensitivity distribution. Two representative cases with fixed τ—$\tau = 10^{-8}$ (blue dashed line) and $\tau = 10^{-4}$ (pink dashed line)—were selected, with their corresponding data shown in subpanel I; here, the pink pentagon denotes the phase transition point. Additionally, two representative cases with fixed N—$N = 20$ (pink solid line) and $N = 36$ (blue solid line)—were selected, with their corresponding data presented in subpanel II, where two five-point stars mark the phase transition points.

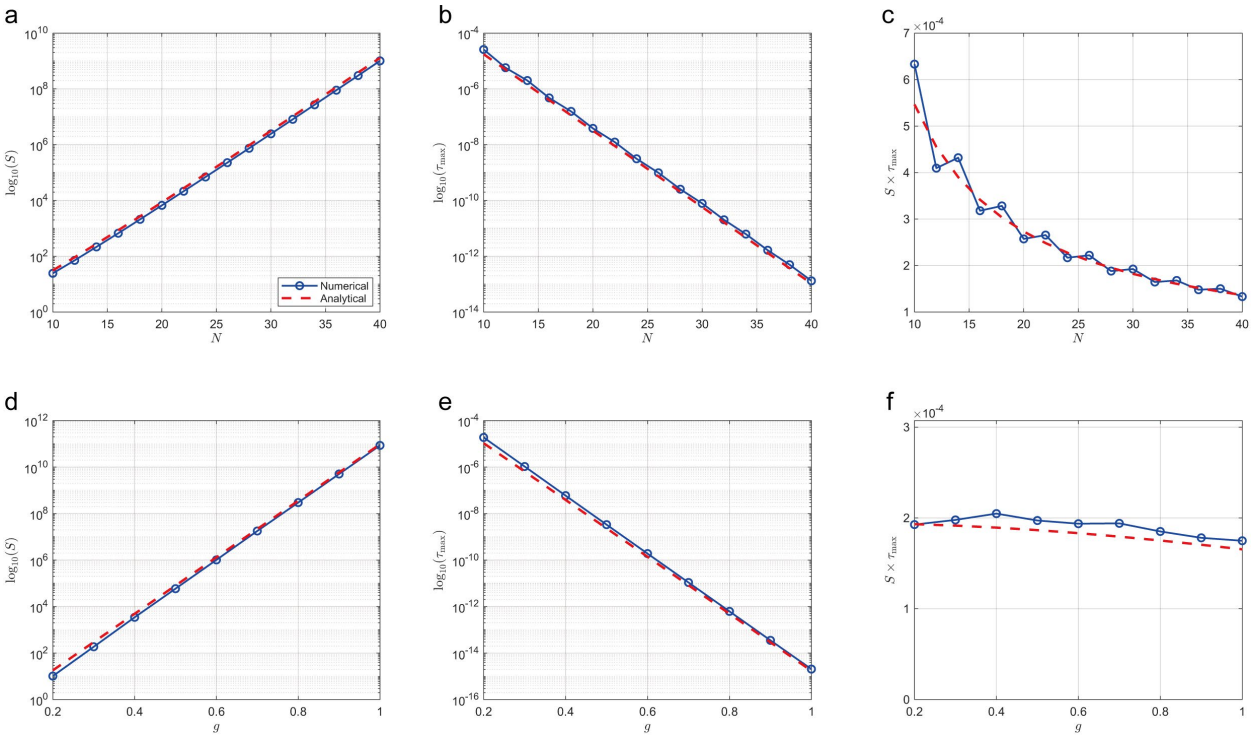

Fig. S7 | Numerical verification of the dual scaling law and the fundamental sensing trade-off for $N/2$-th state in the Hatano-Nelson model. a, b, Evolution of the sensitivity S and dynamic range $\tau_{\max}$ versus the lattice size N at a fixed gauge field strength $g = 0.63$, both exhibiting distinct exponential scaling behaviors. **c,** The sensitivity-dynamic range product $S \times \tau_{\max}$ as a function of N, demonstrating the $1/N$ scaling law constrained by the bulk energy level quantization. **d, e,** Variations of S and $\tau_{\max}$ with respect to the gauge field strength g for a fixed lattice size $N = 30$. **f,** The evolution of the product $S \times \tau_{\max}$ versus g. In all panels, blue dots represent the numerical data, and red dashed lines denote the analytical solutions.

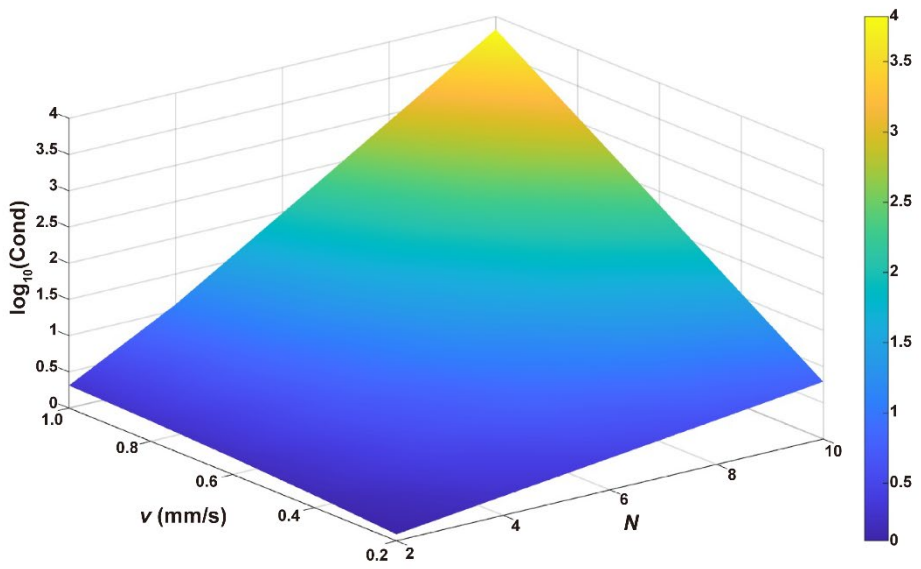

723

724 **Fig. S8 | Sensitivity and stability analysis via the spectral condition number.** The color map illustrates
725 the logarithm of the condition number as a function of the thermal lattice size N and the advective flow
726 velocity v. As N or v increases, the system exhibits an exponential growth in the condition number,
727 indicating that the thermal lattice becomes increasingly non-normal.

728

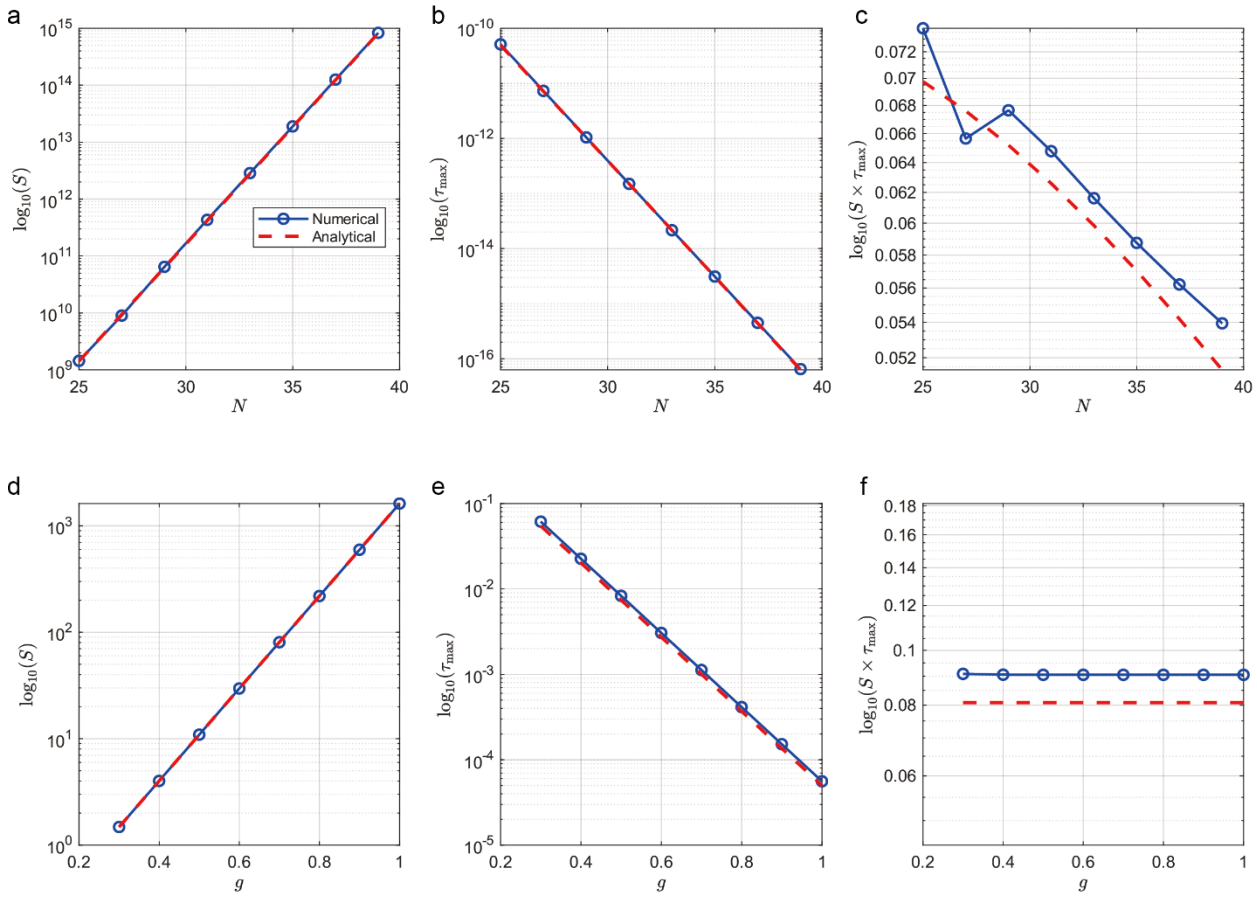

Fig. S9 | Numerical verification of the dual scaling law and the fundamental sensing trade-off for the topological mode in the non-Hermitian SSH model. a, b, Evolution of the sensitivity S and dynamic range $\tau_{\max}$ versus the lattice size N at a fixed gauge field strength $g = 2$, both exhibiting distinct exponential scaling behaviors. **c,** The sensitivity-dynamic range product $S \times \tau_{\max}$ as a function of N, demonstrating the $\propto e^{-N}$ scaling law. **d, e,** Variations of S and $\tau_{\max}$ with respect to the gauge field strength g for a fixed lattice size $N = 21$. **f,** The evolution of the product $S \times \tau_{\max}$ versus g. The flatness of this curve proves the strict cancellation of the non-Hermitian exponential amplification factors within the trade-off relation. In all panels, blue dots represent the numerical data, and red dashed lines denote the analytical solutions.

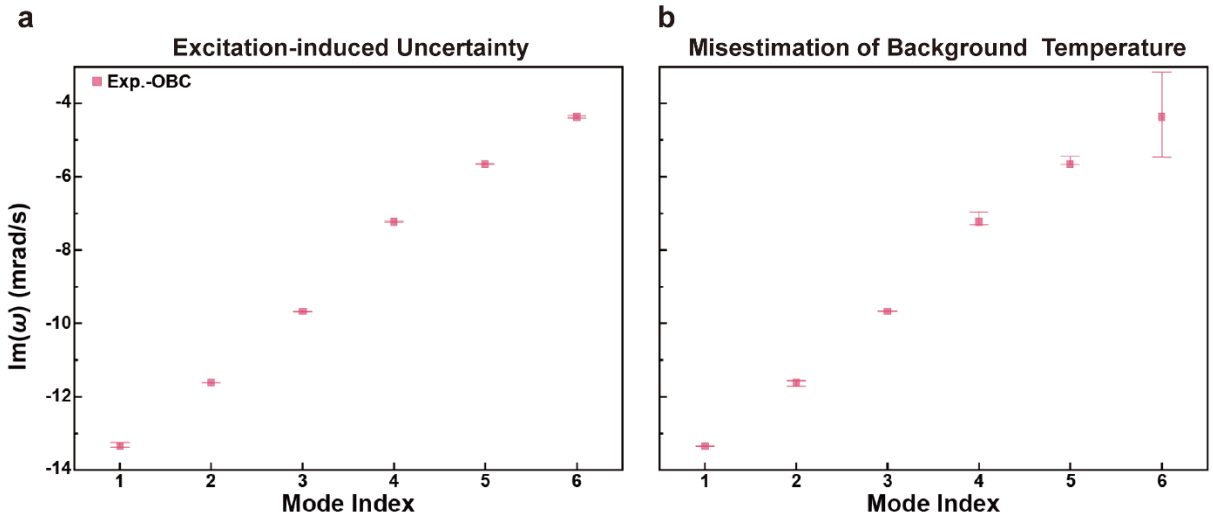

740

741 **Fig. S10 | Robustness tests of the sensor.** Pink rectangles indicate reference values and error bars show

742 uncertainty ranges. **a,** Repeated tests under different heating voltages. **b,** Effect of background temperature

743 misestimation.

744

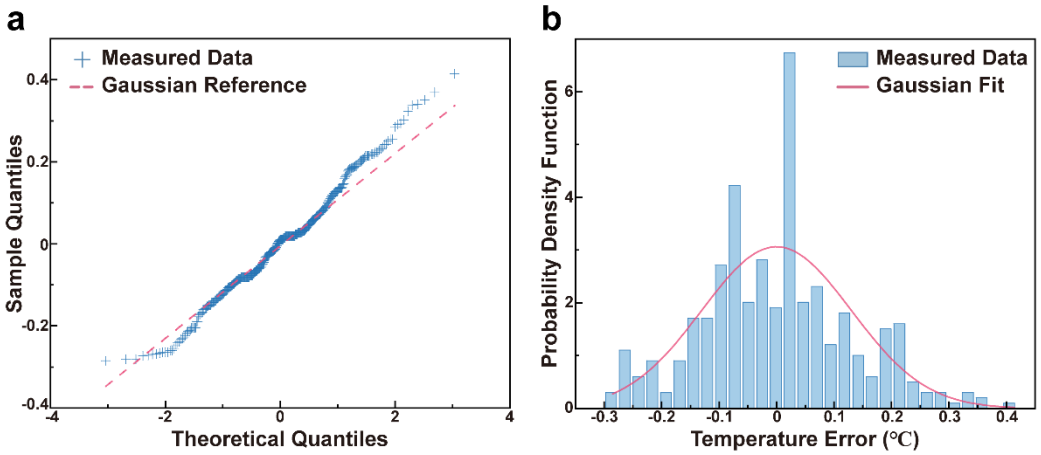

745

746 **Fig. S11 | Noise analysis for the thermal coupling sensor. a**, Quantile-quantile (Q-Q) plot comparing

747 experimental temperature measurements against a Gaussian reference. **b**, Histogram of the experimental

748 measurement error overlaid with a Gaussian fit.

749

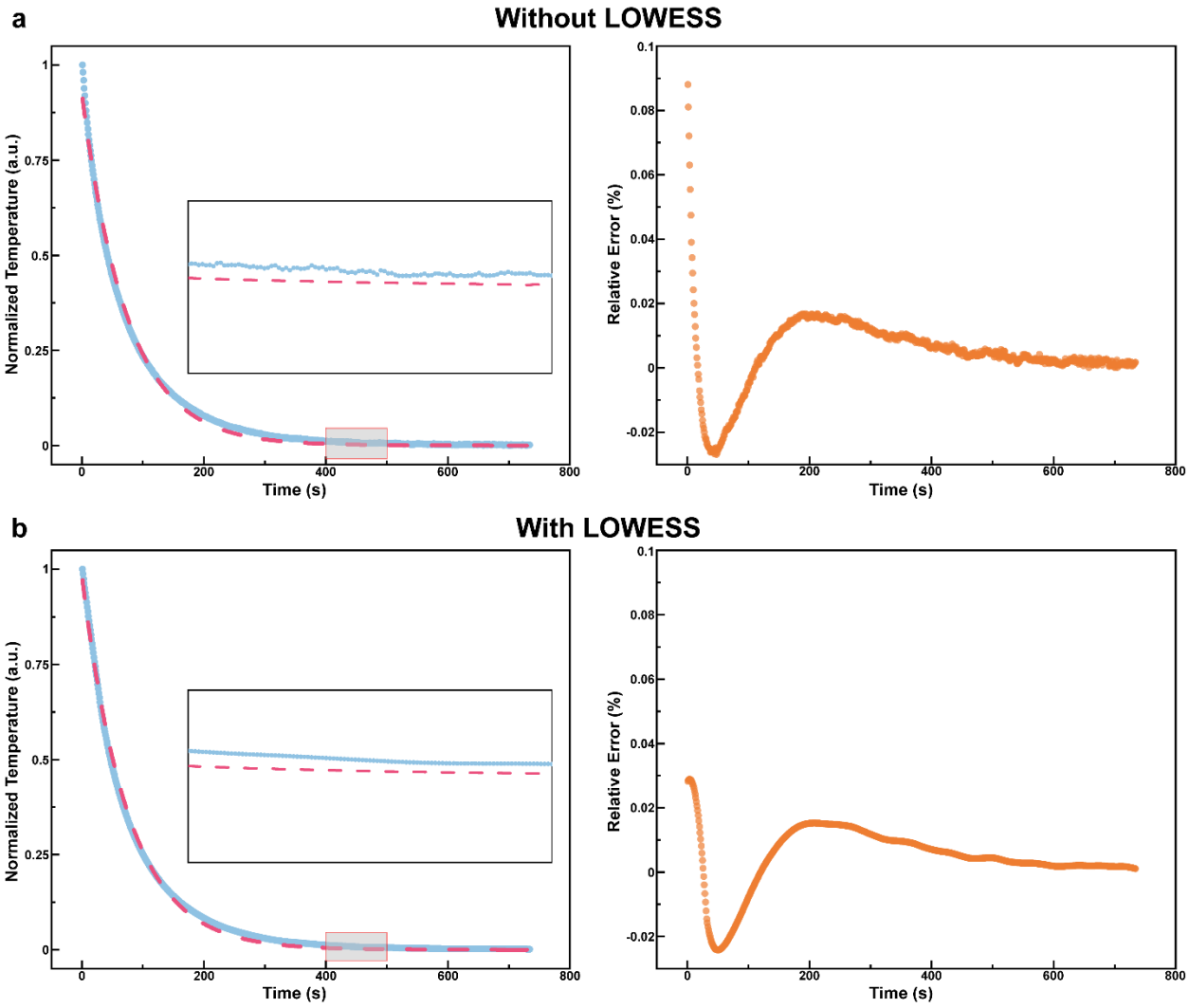

Fig. S12 | Impact of LOWESS pretreatment on the transformation from transient data to frequency-domain eigenvalues. a, Results without LOWESS pretreatment. Left panel: the raw experimental data and the corresponding fitting curve; Right panel: the relative error between the fitting curve and the experimental data. **b**, Results with LOWESS pretreatment. Left panel: the experimental data after LOWESS processing and the resulting fitting curve; Right panel: the relative error between the fitting curve and the processed data.